EFFECT OF ADSORPTION COMPRESSION ON CATALYTIC CHEMICAL REACTIONS

ARPA-E DE-AR0000708 2017 Final Report

Table of Contents

PART II. Demonstration of Catalysis under Adsorption Compression

PART I. Adsorption Compression and Its Influence on Catalytic Chemical Reactions: Theoretical Predictions, Modeling, and Comparisons with Experimental Data

1. Generalized Ono-Kondo Model and Its Application for Analysis of Adsorption Compression

1.1. Thermodynamic fundamentals of Ono-Kondo density functional model

Classical Ono-Kondo model is a density functional theory relating density distribution in adsorbed phase with the bulk density of fluid [1 – 3]. In the simplest versions of this model, adsorbate is semi-infinite one-component lattice system with ε being the energy of interaction between nearest neighbors. Consider taking an adsorbate molecule at a layer i and moving it to an empty site in an infinitely distant layer in the bulk. This is equivalent to the exchange of a molecule with a vacancy [4 – 5],

$$M_i + V \rightarrow V_i + M_b \quad (1)$$

where M is the adsorbate molecule, and V is the vacancy (empty site) that it fills (and vice versa). If this exchange occurs at equilibrium, then:

$$\Delta H - T\Delta S = 0 \quad (2)$$

where ΔH and ΔS are the enthalpy and entropy changes, and T is the absolute temperature.

The value of ΔS can be represented in the form:

$$\Delta S = k \ln W_1 - k \ln W_2 \quad (3)$$

where W_1 is the number of configurations where site in the layer i is occupied by an adsorbate molecule and the site in the infinitely distant layer is empty, W_2 is the number of configurations where the site in the infinitely distant layer is occupied by an adsorbate molecule and site in the layer i is empty, and k is Boltzmann's constant.

If the overall number of configurations for the system is W_0, then:

$$W_1/W_0 = x_i (1 - x_b) \quad (4)$$

and

$$W_2/W_0 = x_b (1 - x_i) \quad (5)$$

where x_i is the fraction of a layer i occupied by molecules of adsorbate, and x_b is the fraction of the bulk phase occupied by adsorbtive molecules.

Substituting equations (4) and (5) into equation (3) we obtain

$$\Delta S = k\, ln[x_i\,(1 - x_b)/(1 - x_i)x_b\,] \qquad (6)$$

The change in enthalpy can be calculated in the mean-field approximation by considering the number of neighboring sites that are occupied near the surface compared to the bulk:

$$\Delta H = -\,\varepsilon\,(z_1 x_{i+1} + z_2\, x_i + z_1 x_{i-1} - z\, x_b\,) \qquad (7)$$

where z_1 is the number of bonds of a molecule with next layer, z_2 is the coordination number in a monolayer, and z is the coordination number in the bulk. From equations (2), (6), and (7) it follows that for $i \geq 2$:

$$ln\{[x_i\,(1 - x_b)]\,/\,[(1 - x_i)x_b]\} + (\varepsilon/kT)[z_1(x_{i+1} - x_b\,) + z_2(x_i - x_b\,) + z_1(x_{i-1} - x_b\,)] = 0 \qquad (8)$$

For $i=1$, we have instead of equation (7):

$$\Delta H = \varepsilon_s - \varepsilon(z_2\, x_1 \; + z_1\, x_2 - z\, x_b\,) \qquad (9)$$

Combining equations (2), (6), and (9), we obtain:

$$ln\{[x_1\,(1 - x_b)]\,/[(1 - x_1)x_b]\} + \varepsilon_s\,/kT + (\varepsilon/kT)(z_2\, x_1 \; + z_1\, x_2 - z\, x_b\,) = 0 \qquad (10)$$

Equation (10) relates density distribution in adsorbed phase with the density in the bulk phase. Various versions of equation (10) allow modeling of various types of adsorption behavior, including adsorption hysteresis [6], order-disorder phase transitions [7], adsorption in micropores [8], and adsorption of supercritical fluids [9]. Based on such modeling, new classification of adsorption isotherms was developed [10].

Equations (8) and (10) are coupled and hence must be solved simultaneously. However, for monolayer adsorption we have $x_i = x_b$ for $i \geq 2$. In this case equation (8) is:

$$ln\{[x_1\,(1 - x_b)]\,/[(1 - x_1)x_b]\} + (\varepsilon/kT)[z_2\, x_1 \; - (z_1 + z_2)\, x_b\,] \; + \; \varepsilon_s\,/kT = 0 \qquad (11)$$

In the low concentration limit, equation (11) gives

$$x_1 = x_b\, exp(-\varepsilon_s\,/kT) \qquad (12)$$

which is Henry's law.

When there are no adsorbate - adsorbate interactions, $\varepsilon = 0$, it follows from equation (11) that

$$x_1 = x_b\,/[x_b + (1 - x_b\,)exp(\varepsilon_s\,/kT)] \qquad (13)$$

which is the Langmuir isotherm widely used in the classical theory of heterogeneous catalysis.

If $x_b << x_1$ then equation (11) gives

$$x_1 = x_b\,/[x_b + (1 - x_b\,)exp(\varepsilon_s\,/kT + z_2\, x_1\, \varepsilon/kT)] \qquad (14)$$

1.2. ***Generalization of the Ono-Kondo techniques for data analysis***

Here we develop a new method allowing application of Ono-Kondo techniques for microporous adsorbents. In addition, this new approach does not require knowing Henry's constants and it is not based on a (mean-field) model of enthalpy for adsorbed molecules.

As seen from equation (7), enthalpy term of Ono-Kondo model is based on lattice model and mean-field approximation. To make Ono-Kondo model more general, consider ΔH in the form of Taylor expansion in powers of density:

$$\frac{\Delta H}{kT} = \frac{\varepsilon_s}{kT} + A_1 x_1 + A_2 x_1^2 + A_3 x_1^3 + \cdots \qquad (15)$$

where

$$A_n = \frac{1}{n!}\frac{\partial^n \Gamma_A}{\partial x_1} \qquad (16)$$

and Γ_A is the energy of intermolecular (adsorbate-adsorbate) interactions.

Plugging $\Delta S = k\, ln[x_1 (1 - x_b)/(1 - x_1) x_b]$ (17)

and ΔH from equation (15) into equation (2) gives:

$$\ln\frac{x_1(1-x_b)}{(1-x_1)x_b} + \frac{\varepsilon_s}{kT} + A_1 x_1 + A_2 x_1^2 + A_3 x_1^3 + \ldots = 0 \qquad (18)$$

Comparison of equation (18) with equation (11) indicates that the coefficient A_1 characterizes energy of adsorbate-adsorbate interaction in the limit of small x_1. In particular, for classical Ono-Kondo model, it becomes $(\varepsilon/kT)z_2$.

Taking into account equation (16), equation (18) can be presented in the following form:

$$\ln\frac{x_1(1-x_b)}{(1-x_1)x_b} = -\frac{\varepsilon_s}{kT} - x_1\Gamma(x_1) \qquad (19)$$

where $\Gamma(x_1) = \Gamma_A + \frac{1}{2!}\frac{\partial \Gamma_A}{\partial x_1} x_1 + \frac{1}{3!}\frac{\partial^2 \Gamma_A}{\partial x_1^2} x_1^2 + \cdots$.

As seen from equation (19), plotting

$$Y = \ln\frac{x_1(1-x_b)}{(1-x_1)x_b} \qquad (20)$$

as a function of x_1 gives information about the sign and the magnitude of intermolecular interactions in adsorbed phase. For example, if the initial slope is negative, then there are repulsions between nearest neighbors at small x_1; if this slope is positive, there are attractions between nearest neighbors at small x_1. For larger x_1, the slope can vary and indicate changes of adsorbate-adsorbate interactions.

Figure 1 illustrates plotting isotherms in coordinates Y vs. x_1 . In Figure 1, predictions of the classical Ono-Kondo equation are represented at $\frac{\varepsilon_s}{kT} = -5$ for two different values of $z_2 \frac{\varepsilon}{kT}$: first is at $z_2 \frac{\varepsilon}{kT} = -2$ (which is attraction) and second is at $z_2 \frac{\varepsilon}{kT} = 2$ (which is repulsion).

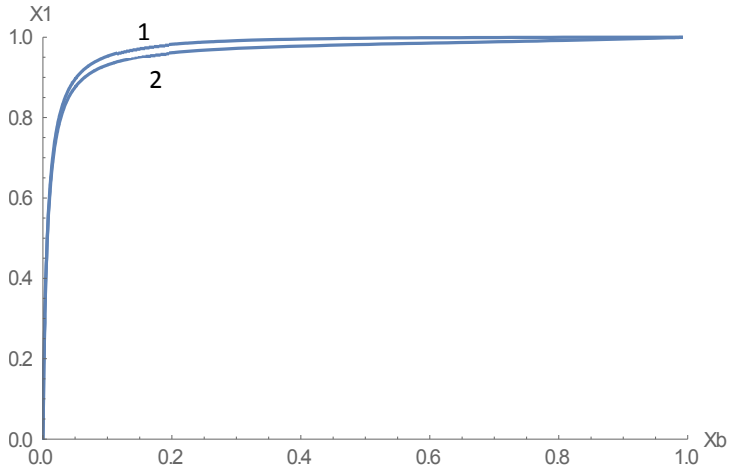

Figure 1. Adsorption isotherms predicted by the classical Ono-Kondo model at $\frac{\varepsilon_s}{kT} = -5$ for two different values of $z_2 \frac{\varepsilon}{kT}$: first is at $z_2 \frac{\varepsilon}{kT} = -2$ (which is attraction) and second is at $z_2 \frac{\varepsilon}{kT} = 2$ (which is repulsion).

As seen from Figure 1, the difference between the two isotherms is not significant at these parameters. To make this difference more pronounced (and measurable), we plot these isotherms in coordinates Y (given by equation (20) vs. x_1, as given by Figure 2.

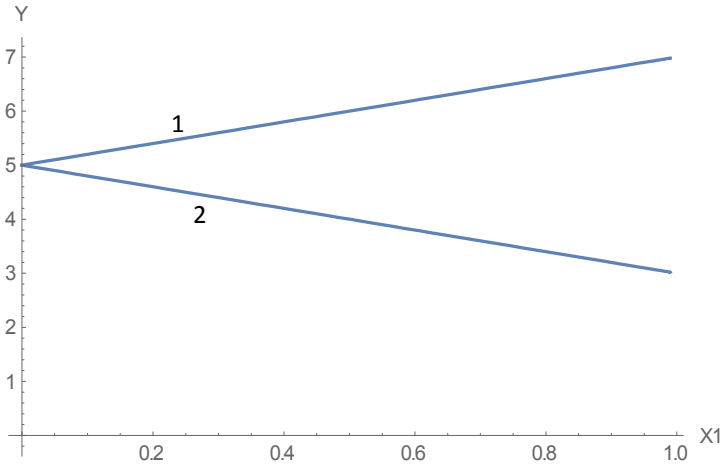

Figure 2. Adsorption isotherms shown in Figure 2 in Ono-Kondo coordinates.

As seen from Figure 2, first isotherm (with attractive adsorbate-adsorbate interactions) has positive slope in this coordinates, and second isotherm (with repulsive adsorbate-adsorbate interactions) has negative slope in this coordinates. So, Ono-Kondo coordinates allow to distinguish between attractive and repulsive interactions, and the absolute value of the slope gives information about the magnitude of those interactions.

Figure 3 illustrates the proposed technique for the classical example of adsorption for ethylene on molecular sieve 13X at 50 C [17]. In Figure 3, adsorption isotherm is plotted as Y (given by equation (20)) vs x_1.

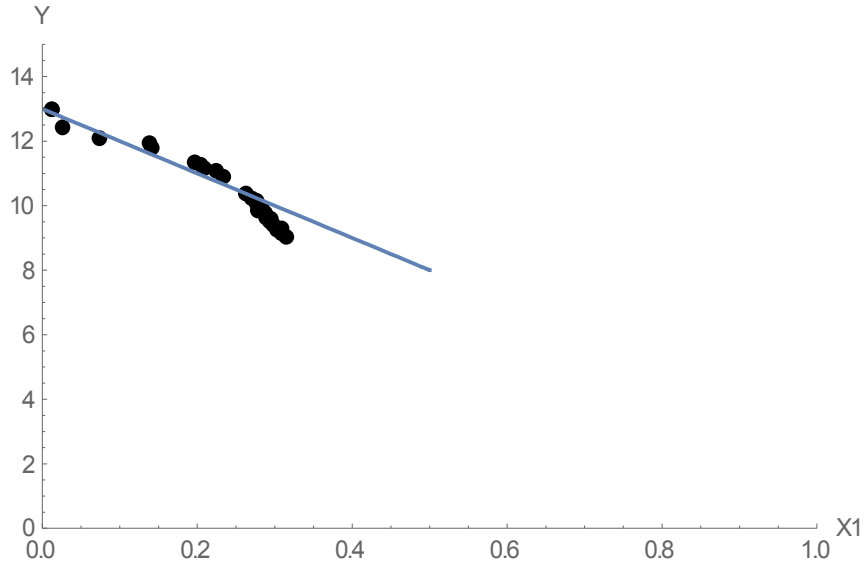

Figure 3. Adsorption isotherm for ethylene on molecular sieve 13X at 50 C in coordinates of equation (19): Y (in units of RT) versus adsorbate density, X1. Experimental data from [17].

As seen from Figure 3, the slope at small x_1 is negative and A_{11} is about $13RT$, which gives energy of adsorbate-adsorbate interactions about 35 KJ/mol. It is remarkable that the slope of the curve on Figure 3 is negative starting from zero adsorption. Since negative slope indicates repulsions, this result demonstrates that a nano-pore can "accommodate" only one molecule of ethylene without compression. However, each neighbor will cause adsorbate-adsorbate repulsions. Therefore, adsorption compression starts from low densities.

1.3. Application of the new Ono-Kondo techniques for adsorption of NO on exfoliated graphite

To illustrate the difference between adsorption of NO on flat surface and in nano-porous zeolite, consider example of NO adsorption on exfoliated graphite [22]. Figure 4 shows experimental isotherm for this case at T = 77.3 K.

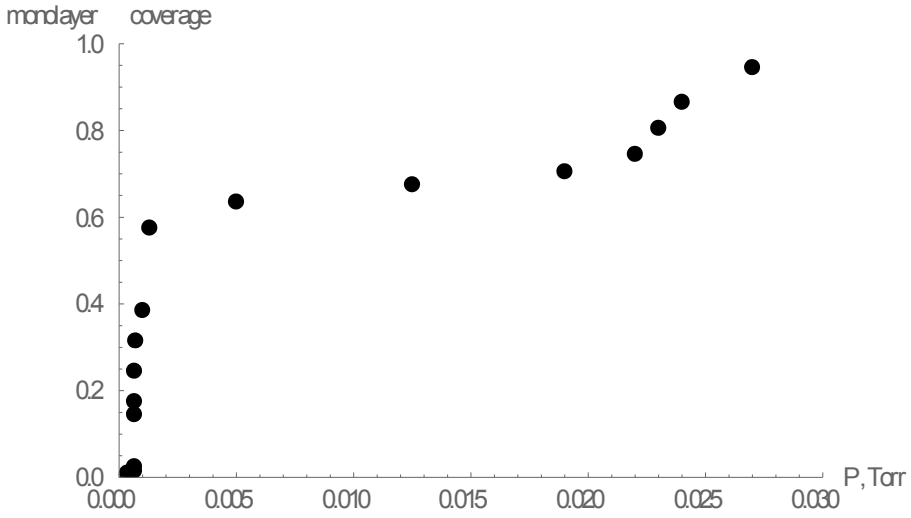

Figure 4. Adsorption isotherm for NO on exfoliated graphite at T = 77.3 K. Data from [22].

Figure 5 gives this isotherm in normalized coordinates.

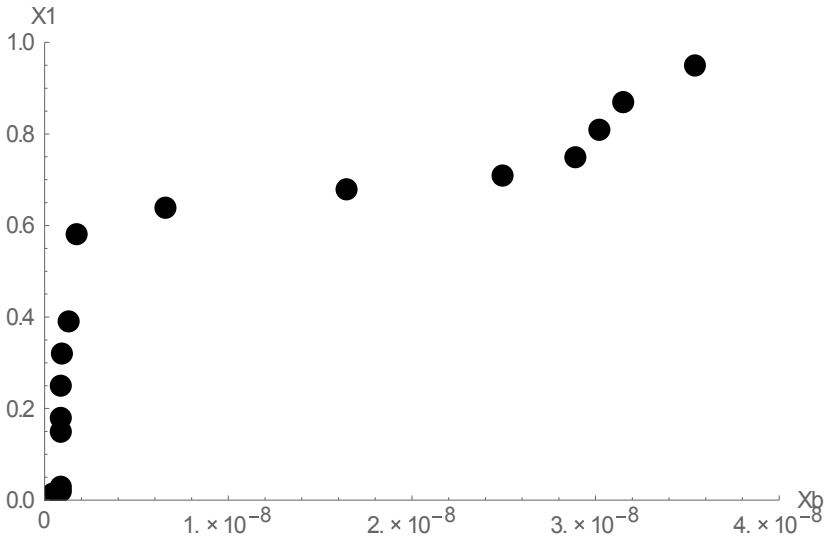

Figure 5. Adsorption isotherm for NO on exfoliated graphite at T = 77.3 K in normalized coordinates. Data from [22].

Figure 6 shows data presented in Figures 4 and 5 in coordinates of equation (19).

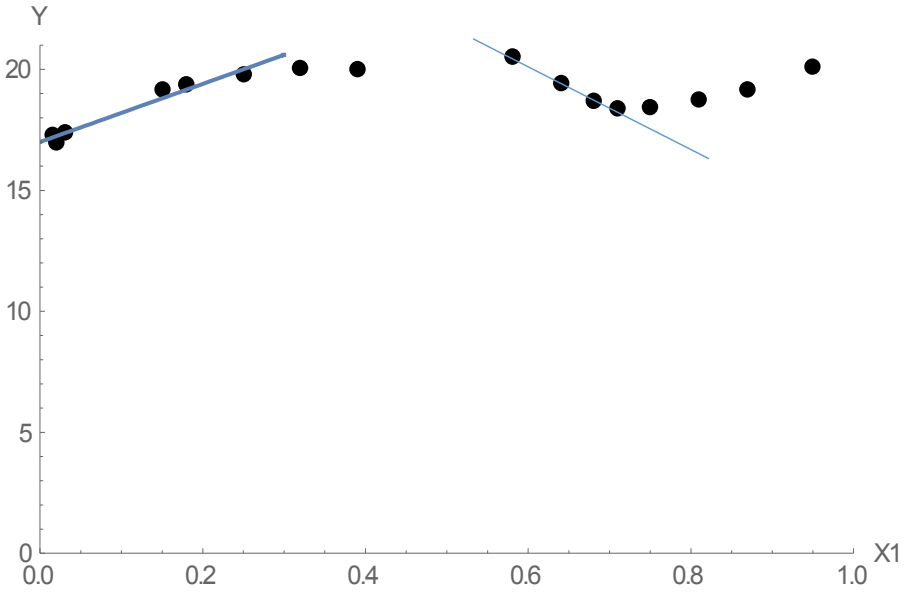

Figure 6. Adsorption isotherm for NO on exfoliated graphite at T = 77.3 K in coordinates of equation (19). Data from [22].

As seen from Figure 6, at low densities the slope is positive which indicates adsorbate-adsorbate attractions. This is consistent with a classical concept of adsorption on a flat surface. However, at normalized density between 0.6 and 0.8, there is a negative slope indicating repulsions. These results are consistent with the independent study by neutron scattering [22] showing transition from two-dimensional liquid to two-dimensional solid.

2. Application of the new Ono-Kondo techniques to determine adsorption compression for NO in nano-porous zeolites

Analysis of literature indicates that there are few publications reporting on adsorption isotherms for nitric oxide (NO) on nano-porous zeolites. In recent papers by Yi, Deng et al [20, 21], the authors presented adsorption isotherms for NO on zeolites (NaX, NaY, CaA, and 5A) and found significant deviations from Langmuir's behavior (see, for example, Figure 3 in ref. [20]). Since Ono-Kondo technique allows to analyze deviations from Langmuir's behavior and allows to determine energies of adsorbate-adsorbate interactions, we plotted these isotherms in coordinates of equation (19).

The problem of using equation (19) for microporous adsorbents is finding adsorption capacity for normalization of adsorption amount. However, BET method is not applicable for microporous adsorbents (see, for example, IUPAC documents [23, 24]), and there is no reliable method to determine surface areas for them. This is because BET model is set for macropores with flat surfaces and adsorption compression changes area per molecule; in addition, surface area measured at 77 K does not reflect adsorption capacity at catalytic conditions, such as T > 300 K. For this reason, we developed a new approach where knowing adsorption capacity is not necessary to plot data in coordinates of equation (19). In this approach, we consider systems where adsorbed amount is relatively small (micromoles per gram), which is typical for adsorption of supercritical NO on zeolites (critical temperature for NO is 180 K). In this case,

$$x_1 \ll 1 \qquad (21)$$

and

$$x_b \ll 1 \qquad (22)$$

With conditions (21) and (22), equation (19) can be transformed to the following:

$$\ln\frac{x_1}{x_b} = -\frac{\varepsilon_s}{kT} - x_1\Gamma_A \tag{23}$$

Plugging

$$x_1 = a/a_m \tag{24}$$

in equation (23) gives:

$$\ln\frac{a/a_m}{x_b} = -\frac{\varepsilon_s}{kT} - (a/a_m)\Gamma_A \tag{25}$$

Since adsorption capacity is adsorption at the point where attraction to adsorbent is compensated by repulsions from neighboring molecules of adsorbate, at this point ΔH = 0, which results in

$$\frac{\varepsilon_s}{kT} + x_1^*\frac{E_{rep}}{kT} = 0 \tag{26}$$

where E_{rep} is the energy of repulsion, x_1^* is x_1 at $a = a_m$, i.e. $x_1^* = 1$, which gives instead of equation (26):

$$\frac{\varepsilon_s}{kT} + \frac{E_{rep}}{kT} = 0 \tag{27}$$

Plugging $\Gamma_A = \frac{E_{rep}}{kT}$ in equation (25) and eliminating $\frac{\varepsilon_s}{kT}$ by using equation (27) gives:

$$\ln\frac{a}{x_b} = \ln(a_m) + \frac{E_{rep}}{kT} - \frac{E_{rep}}{a_m kT}a \tag{28}$$

As seen from equation (28), plotting $ln(a/x_b)$ vs a allows to get the slope, S, and the intercept, I, which are:

$$S = -\frac{E_{rep}}{a_m kT} \tag{29}$$

$$I = \ln(a_m) + \frac{E_{rep}}{kT} \tag{30}$$

Knowing S and I from plotting experimental data allows to solve equations (29) and (30) with respect to $\frac{E_{rep}}{kT}$ and a_m. So, the proposed method gives the energy of adsorbate-adsorbate intermolecular interactions without knowing adsorption capacity. In addition, this procedure gives actual adsorption capacity, a_m. In fact, excluding $\frac{E_{rep}}{kT}$ from equations (29) and (30) results in the following equation for determining a_m:

$$\ln(a_m) - Sa_m - I = 0 \tag{31}$$

Note that, in equation (31), units of a_m are the same as units of a.

2.1. ***NO on NaX***

Figure 7 gives the adsorption isotherm for NO on zeolite NaX measured at T = 323 K by static volumetric apparatus [20]. At this temperature, NO is supercritical, and at pressures below 70 kPa, adsorption amounts are very small (micromoles per gram) which allows using equation (28).

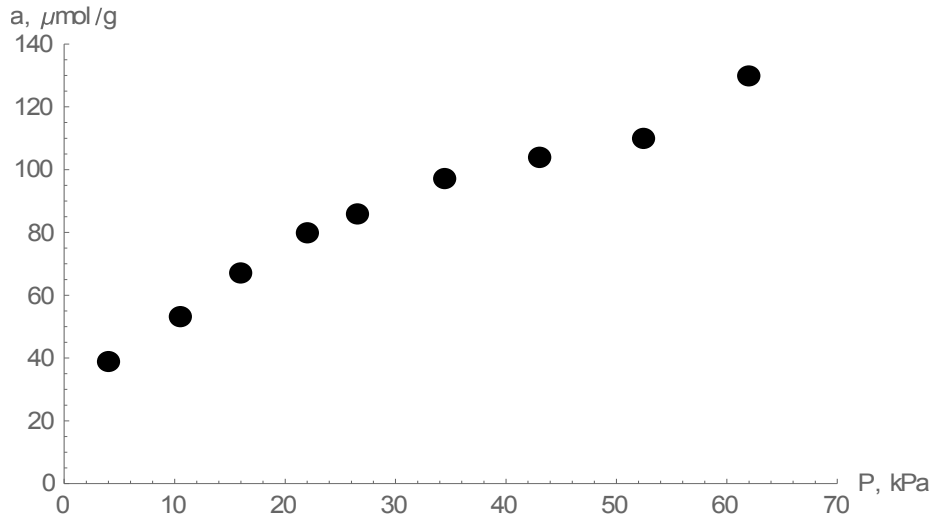

Figure 7. Adsorption isotherm for NO on zeolite NaX measured by static volumetric apparatus at T = 323 K. Data from [20].

Figure 8 shows the adsorption isotherm for NO on NaX (shown in Fig. 7) in coordinates *a [μmol/g]* vs x_b. This is necessary to plot this isotherm in coordinates of equation (28).

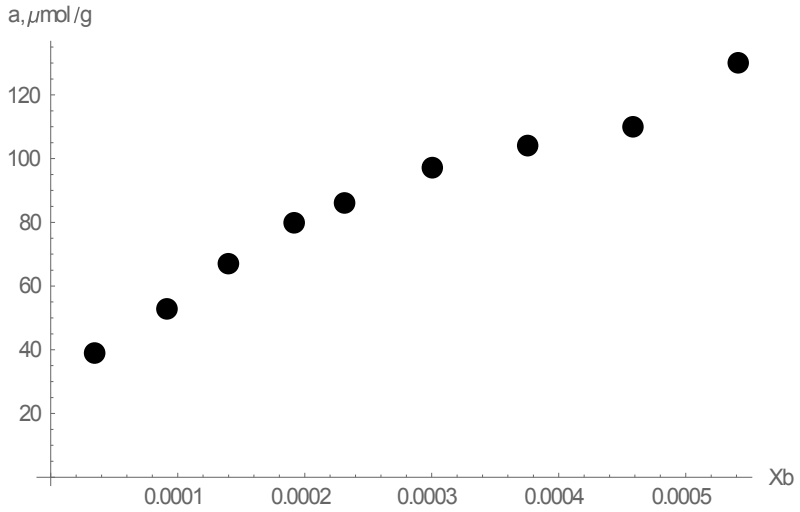

Figure 8. Adsorption isotherm for NO on zeolite NaX at T = 323 K in coordinates *a [μmol/g]* vs x_b.

Figure 9 gives adsorption isotherm, presented in Figure 8, in coordinates of equation (28), i.e. $Y = ln(a/x_b)$ vs a. Lower frame shows this plot in a larger scale.

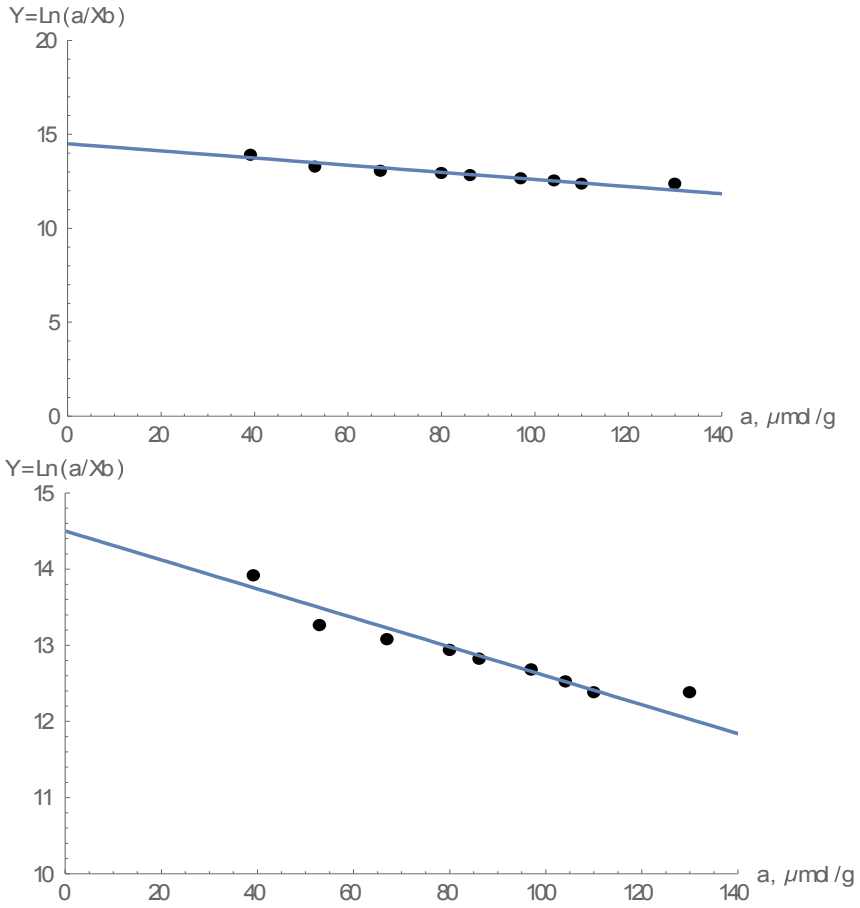

Figure 9. Adsorption isotherm for NO on zeolite NaX in coordinates of equation (28). Upper and lower frames show the isotherm in different scales.

As seen from Figure 9, the slope is negative (repulsions) which indicates adsorption compression. From Figure 9, the slope, $S \approx -0.019$ and the intercept, $I \approx 14.5$. With these S and I, equation (31) gives $a_m \approx 442.5$ *μmol/g*. Then, energy of adsorption compression is $\frac{E_{rep}}{kT} \approx 8.04$ which corresponds to $E_{rep} \approx 5.194$ *kCal/mol*. Figure 10 shows the same isotherm in coordinates of equation (19) without approximations (21) and (22), where adsorption capacity is $a_m \approx 442.5$ *μmol/g* (determined from Figure 9).

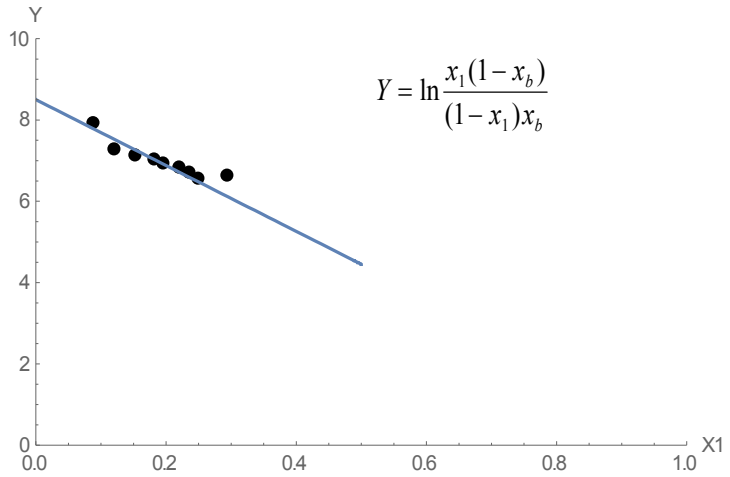

Figure 10. Adsorption isotherm for NO on zeolite NaX in coordinates of equation (19).

*2.2. **NO on CaA and on NaY***

Figure 11 shows adsorption isotherms for NO on zeolites CaA and NaY measured by static volumetric apparatus at T = 323 K. Figure 12 gives this adsorption isotherm in coordinates *a [μmol/g]* vs x_b. This is necessary to plot this isotherm in coordinates of equation (28).

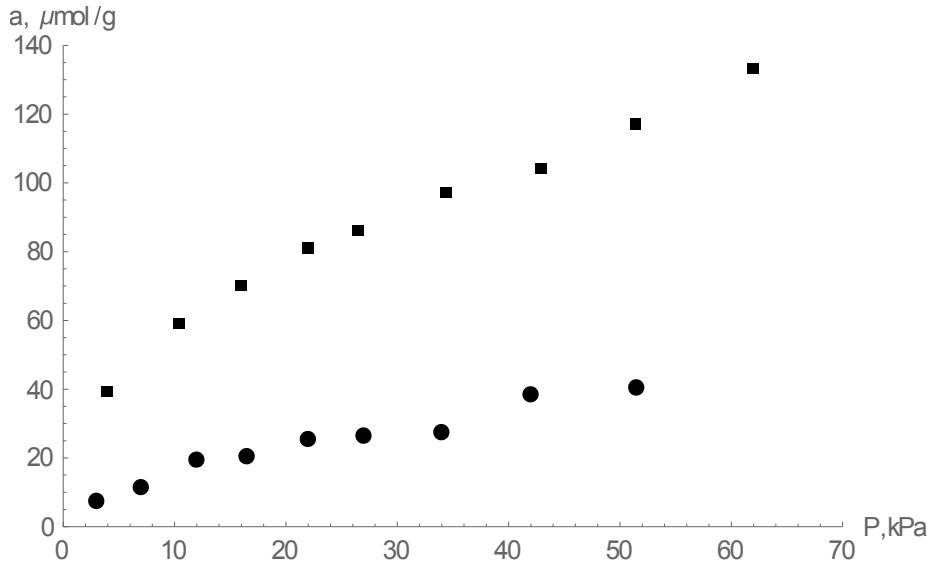

Figure 11. Adsorption isotherms for NO on zeolites CaA (■) and NaY (●) measured by static volumetric apparatus at T = 323 K. Data from [20].

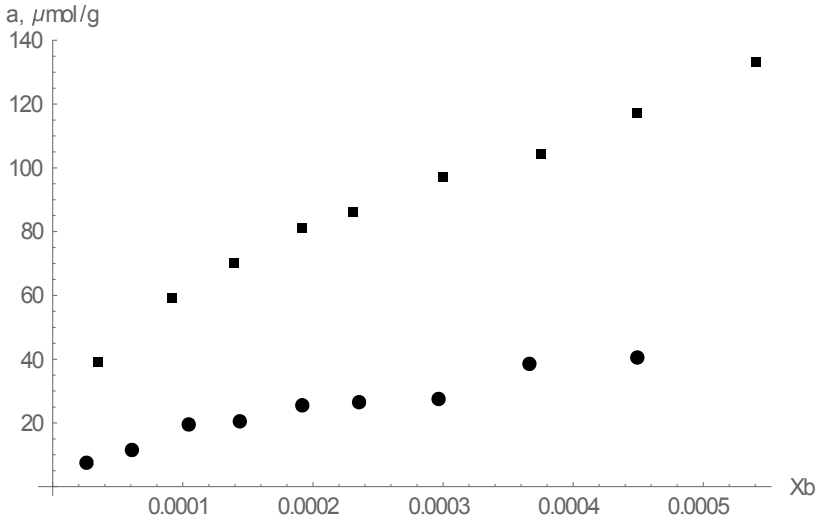

Figure 12. Adsorption isotherms for NO on zeolites CaA (■) and NaY (●) at T = 323 K in coordinates *a [μmol/g]* vs x_b.. Data from [20].

Figure 13 gives this adsorption isotherm in coordinates of equation (28), $ln(a/x_b)$ vs a.

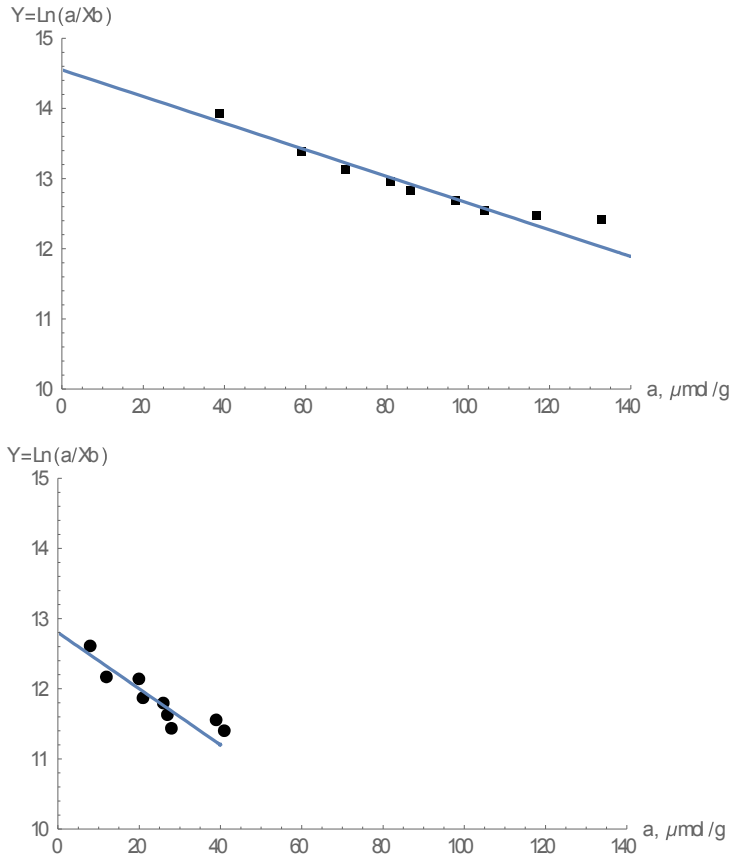

Figure 13. Adsorption isotherms for NO on zeolites CaA (■) and NaY (●) in coordinates of equation (28). Data from [20].

As seen from Figure 13 the slopes for both CaA and NaY are negative (repulsions) which indicates adsorption compression. From Figure 13, the slopes are - *0.019* (for CaA) and - *0.04* (for NaY). The intercepts are *14.55* (for CaA) and 12.8 (for NaY). With these *S* and *I*, equation (31) gives $a_m \approx 444.85\ \mu mol/g$ (for CaA) and $a_m \approx 188.96\ \mu mol/g$ (for NaY). Then, energy of adsorption compression is $\frac{E_{rep}}{kT} \approx 8.45$ (for CaA) and $\frac{E_{rep}}{kT} \approx 7.56$ (for NaY). This corresponds to $E_{rep} \approx 5.46\ kCal/mol$ (for CaA) and $E_{rep} \approx 4.88\ kCal/mol$ (for NaY). Figure 14 shows the same isotherms in coordinates of equation (19) without approximations (21) and (22), where adsorption capacities are $a_m \approx 444.85\ \mu mol/g$ for CaA and $a_m \approx 188.96\ \mu mol/g$ for NaY (determined from Figure 13).

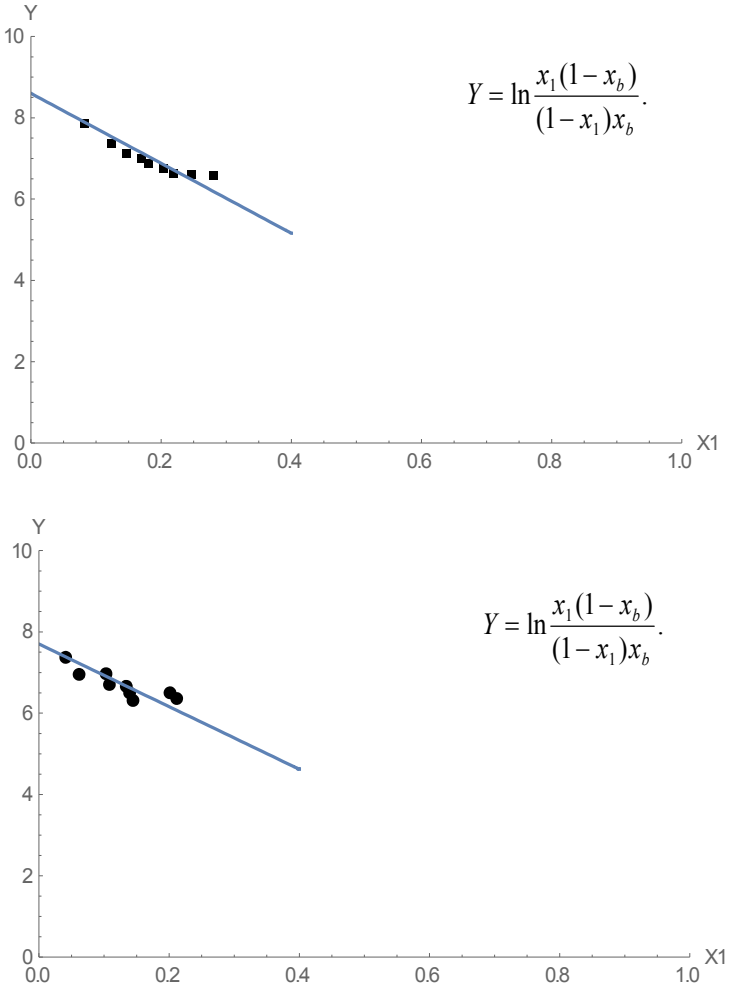

Figure 14. Adsorption isotherms for NO on zeolites CaA (■) and NaY (●) in coordinates of equation (19).

*2.3. **NO on 5A***

Figure 15 gives the adsorption isotherms for NO on zeolite 5A measured by static volumetric apparatus at various temperatures [21]: 323 K (●), 348 K (♦), and 363 K (■). Figure 16 gives this adsorption isotherm in coordinates *a [μmol/g]* vs x_b. This is necessary to plot this isotherm in coordinates of equation (28).

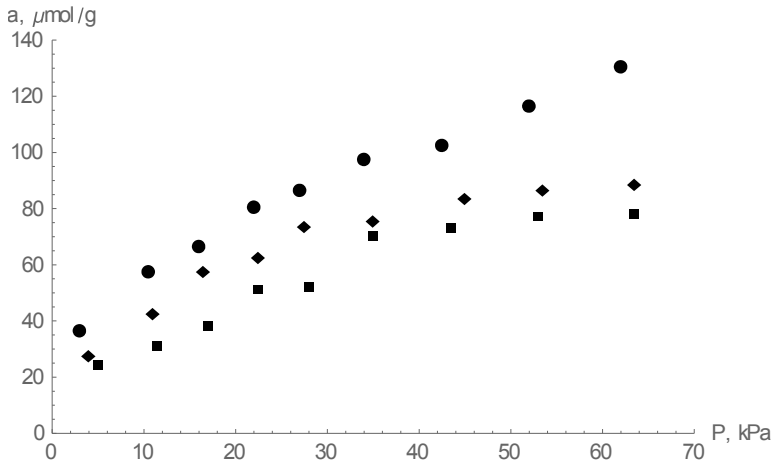

Figure 15. Adsorption isotherms for NO on zeolite 5A measured by static volumetric apparatus at various temperatures: 323 K (●), 348 K (♦), and 363 K (■). Data from [21].

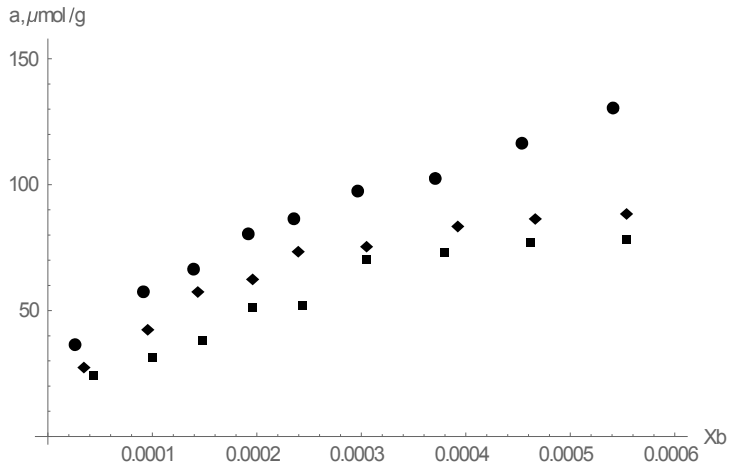

Figure 16. Adsorption isotherms for NO on zeolite 5A in coordinates *a [μmol/g]* vs x_b.: 323 K (●), 348 K (♦), and 363 K (■). Data from [21].

Figure 17 gives adsorption isotherms for NO on zeolite 5A at various temperatures in coordinates of equation (28), $ln(a/x_b)$ vs a. As seen from Figure 17, the slopes are negative (repulsions) which indicates adsorption compression. From Figure 17, the slopes are - *0.02* (for T = 323 K), - *0.022* (for T = 348 K), and - *0.024* (for T = 363 K). The intercepts are *14.7* (for T = 323 K), *14.1* (for T = 348 K), and *13.8* (for T = 363 K). With these S and I, equation (31) gives $a_m \approx 431.62\ \mu mol/g$ (for T = 323 K), $a_m \approx 371.88\ \mu mol/g$ (for T = 348 K), and $a_m \approx 332.995\ \mu mol/g$ (for T = 363 K). Then, the energy of adsorption compression is $\frac{E_{rep}}{kT} \approx 8.63$ (for T = 323 K), $\frac{E_{rep}}{kT} \approx 8.18$ (for T = 348 K), and $\frac{E_{rep}}{kT} \approx 7.99$ (for T = 363 K). This corresponds to $E_{rep} \approx 5.58\ kCal/mol$ (for T = 323 K), $E_{rep} \approx 5.69\ kCal/mol$ (for T = 348 K), and $E_{rep} \approx 5.8\ kCal/mol$ (for T = 363 K). Figure 18 shows the same isotherms in coordinates of equation (29) without approximations (21) and (22), where adsorption capacities are $a_m \approx 431.62\ \mu mol/g$ for T = 323 K, $a_m \approx 371.88\ \mu mol/g$ for T = 348 K, and $a_m \approx 332.995\ \mu mol/g$ for T = 363 K (determined from Figure 17).

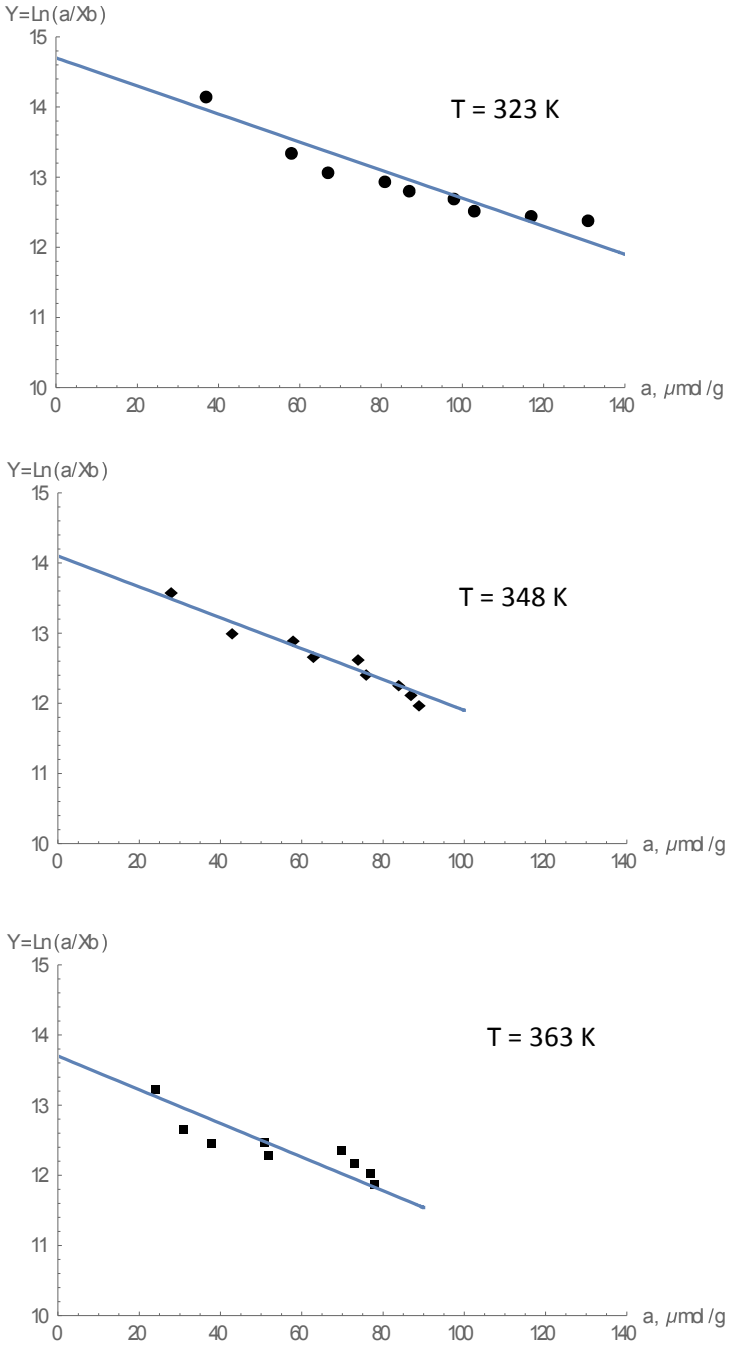

Figure 17. Adsorption isotherm for NO on zeolite 5A at T = 323 K, T = 348 K, and T = 363 K in coordinates of equation (28).

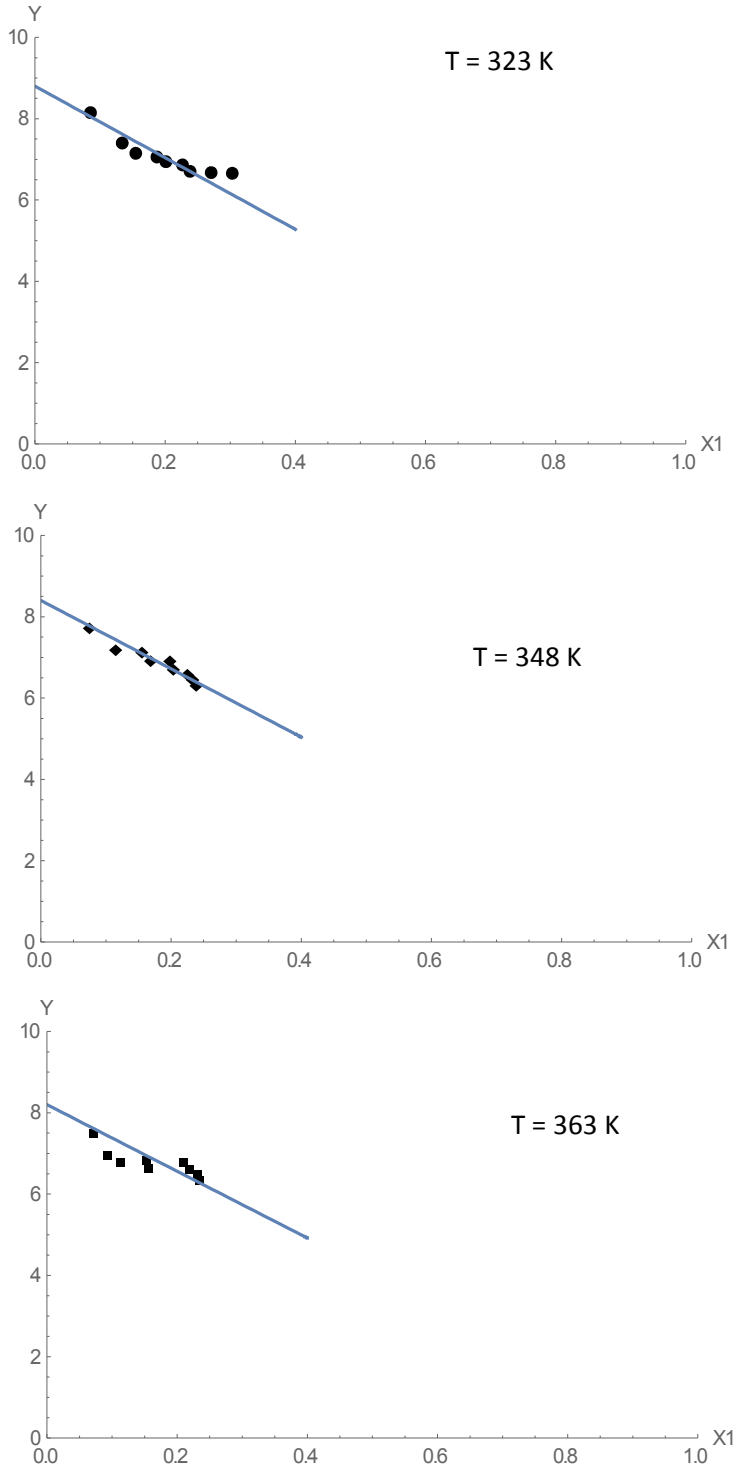

Figure 18. Adsorption isotherms for NO on zeolite 5A at T = 323 K, T = 348 K, and T = 363 K in coordinates of equation (19). In this Figure, $Y = \ln \frac{x_1(1-x_b)}{(1-x_1)x_b}$.

2.4. N_2 on ZSM-5

Measurements of adsorption isotherms for N_2 on zeolite ZSM-5 were performed on BET apparatus Micromeritics 2010. Zeolite sample ratio of Si/Al was 11.5, and sample weight 0.09 g.

Figure 19 shows adsorption isotherm for N_2 on ZSM-5 at T = 77 K. This isotherm was plotted in coordinates of generalized Ono-Kondo equation.

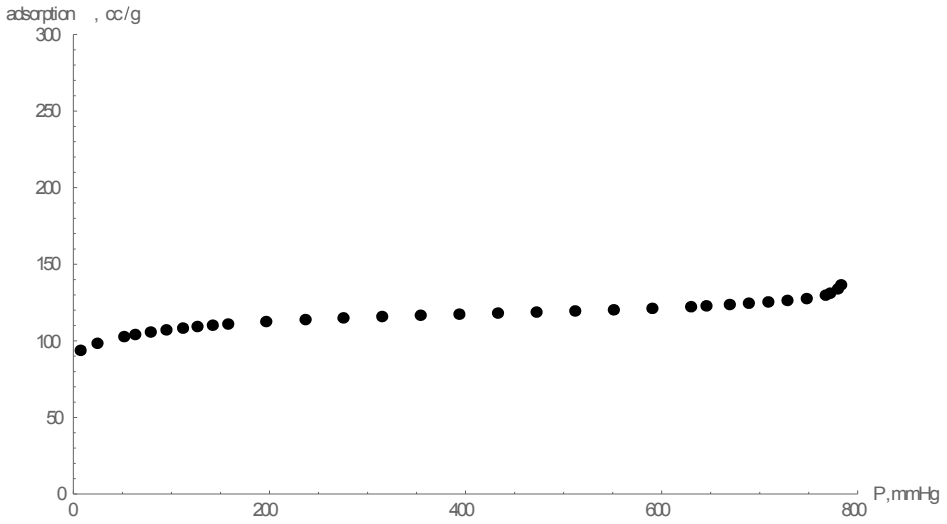

Figure 19. Adsorption isotherm for N_2 on ZSM-5 (Si/Al = 11.5) obtained on BET apparatus at T = 77 K.

Figure 20 gives adsorption isotherm for N_2 on zeolite ZSM-5 in coordinates of equation (28).

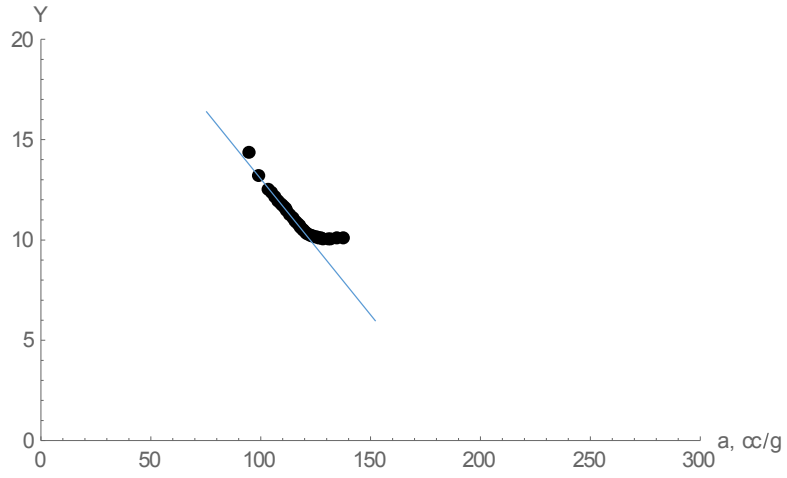

Figure 20. Adsorption isotherm for N_2 on ZSM-5 (Si/Al = 11.5) in coordinates of equation (28).

As seen from Figure 20, the slope is negative (repulsions) which indicates adsorption compression. From Figure 20, the slope is – *0.12* and the intercept is about 26.5. With these *S* and *I*, equation (31) gives $a_m \approx 180$ *cc/g*. Then, energy of adsorption compression is $\frac{E_{rep}}{kT} \approx 21.6$ which corresponds to $E_{rep} \approx 3.3$ *kCal/mol*. Figure 21 shows the same isotherm in coordinates of equation (19) without approximations (21) and (22), where adsorption capacity is $a_m \approx 180$ *cc/g* (determined from Figure 20). Note that these techniques allow processing of isotherms in the original units of BET apparatus, adsorption in cc/g and pressure in mm Hg.

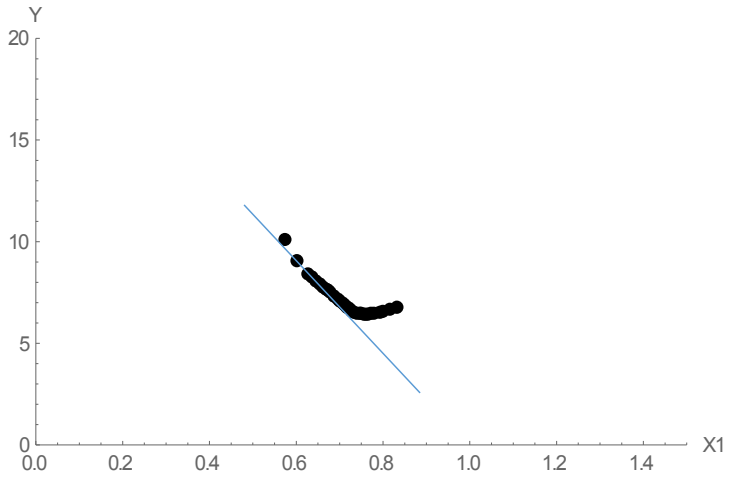

Figure 21. Adsorption isotherm for N_2 on ZSM-5 (Si/Al = 11.5) in coordinates of equation (19).

3. Energies of adsorption compression for NO on zeolites

Table 1 shows energies of adsorption compression for NO on various zeolites obtained from Figures 7 – 18. Table 1 also shows information on pores sizes distribution known from nitrogen adsorption and from small angle X-ray scattering (SAXS) [32].

Table 1. Energies of adsorption compression for NO on zeolites obtained from Figures 7 – 18.

Zeolites	T, K	Pore size distribution, Å *	Energy of adsorption compression
NaX	323 K	2 Å … 15 Å	5.2 kCal/mol
NaY	323 K	3 Å … 14 Å	4.88 kCal/mol
CaA	323 K	2 Å … 15 Å	5.46 kCal/mol
5A	323 K	Narrow around 5 Å	5.6 kCal/mol
5A	348 K	Narrow around 5 Å	5.7 kCal/mol
5A	363 K	Narrow around 5 Å	5.8 kCal/mol

Table 2 shows activation enthalpies for NO oxidation on Silica, SIL-1, SIL-1D, BEA, and CHA zeolites at 278 – 373 K [33].

Table 2. Activation enthalpies for NO oxidation on Silica, SIL-1, SIL-1D, BEA, and CHA zeolites at 278–373 K [33].

Zeolites	Activation enthalpies for NO on zeolites
Silica	7.42 ± 1.1 kCal/mol
SIL-1	8.56 ± 0.5 kCal/mol
SIL-1D	9.45 ± 0.19 kCal/mol
BEA	8.97 ± 2.97 kCal/mol
CHA	9.86 ± 0.33 kCal/mol

As seen from comparisons of Tables 1 and 2, energies of adsorption compression are comparable with activation enthalpies of zeolites.

4. Thermodynamic capacity of catalysts

4.1. ***Grand Canonical Model***

As seen from the section on NO on zeolites, at T = 323 K estimated values of a_m for NaX, NaY, and CaA are about 440 μmol/g. If area per one molecule of NO is 19 Å^2, than the surface area is about 50 m^2/g which is at least an order of magnitude less than that of BET surface areas for these adsorbents. This difference comes from the fact that the value of a_m in equation (28) is adsorption at the point where attraction to the surface is compensated by repulsions between adsorbate molecules. Therefore, it is an actual (thermodynamic) capacity, not geometrical capacity which can be expected from BET measurements (not to mention that BET model is incorrect for microporous adsorbents [23, 24]).

To illustrate the concept of thermodynamic capacity, consider a simplest situation where adsorption compression is possible and which allows rigorous theoretical treatment [31]: two active sites at various distances, as shown in Figure 22.

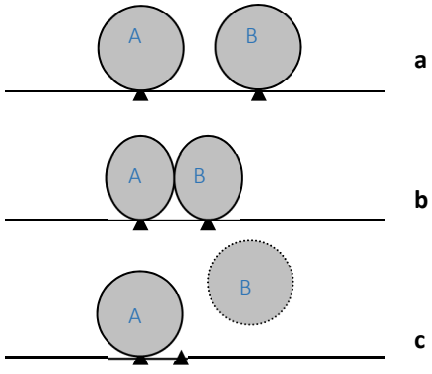

Figure 22. Molecules on active sites

When the active sites are close and their attraction of adsorbate molecules is strong, both sites can be occupied, but the adsorbed molecules will repel each other (Figure 22b). In this case, attraction to the active sites must be stronger than repulsion between neighbors. Therefore, adsorption of both molecules simultaneously is thermodynamically favorable; however, the distance between such molecules is smaller than in a normal liquid and adsorbate molecules

repel each other. This is the simplest case of the adsorption compression, and it can occur whenever the lattice spacing for molecules in the adsorbent is smaller than the minimum in the potential function for adsorbate – adsorbate interactions. At very small distances between active sites (Figure 22c), this effect disappears: the A molecule blocks the neighboring active site because repulsions between neighbors exceeds attractions to the active sites at this distance.

For the grand canonical ensemble, the variables are chemical potential, μ, number of molecules on active sites, N, and absolute temperature, T. To calculate the grand canonical partition function, Ξ, we assume that a gas phase is in equilibrium with two active sites with ε_s being the energy of molecule-active site interactions, and d being the distance between sites. For this model, there are four different states:

- one state with both active sites empty; configurational energy of this state is zero;
- two states where only one of sites is occupied; configurational energy of each of these states is ε_s ;
- one state where both sites are occupied and the interaction energy between molecules sitting on these sites is $\varphi(d)$:

$$\varphi(d) = 4\varepsilon[(\frac{\sigma}{d})^6 - (\frac{\sigma}{d})^{12}] \tag{32}$$

Configurational energy of this state is $2\varepsilon_s + \varphi(d)$.

The grand canonical partition function for this system can be written as:

$$\Xi = \exp(-\frac{E_0}{kT}) + \exp(\frac{\mu}{kT} - \frac{E_1^{'}}{kT}) + \exp(\frac{\mu}{kT} - \frac{E_1^{''}}{kT}) + \exp(\frac{2\mu}{kT} - \frac{E_2}{kT}) \tag{33}$$

where k is Boltzmann's constant, and:

$$E_0 = 0 \tag{34}$$

$$E_1^{'} = E_1^{''} = \varepsilon_s \tag{35}$$

$$E_2 = 2\varepsilon_s + \varphi(d) \tag{36}$$

The average number of molecules, $<<N>>$, sitting on the two active sites is:

$$<< N >>= \frac{1}{\Xi}[\exp(\frac{\mu}{kT} - \frac{E_1^{'}}{kT}) + \exp(\frac{\mu}{kT} - \frac{E_1^{''}}{kT}) + 2\exp(\frac{2\mu}{kT} - \frac{E_2}{kT})] \tag{37}$$

Plugging equations (33) – (36) into equation (37) gives:

$$<< N >>= \frac{2\exp(\frac{\mu}{kT} - \frac{\varepsilon_s}{kT}) + 2\exp[\frac{2\mu}{kT} - \frac{2\varepsilon_s}{kT} - \frac{\varphi(d)}{kT}]}{1 + 2\exp(\frac{\mu}{kT} - \frac{\varepsilon_s}{kT}) + \exp[\frac{2\mu}{kT} - \frac{2\varepsilon_s}{kT} - \frac{\varphi(d)}{kT}]} \tag{38}$$

*4.2. **Thermodynamic Capacity versus Geometrical (BET) Capacity***

Figure 23 gives adsorption isotherm predicted by equation (38) at $\varepsilon/kT = -0.5$, $\varepsilon_s/kT = -15$, $\sigma = 3.5$ Å, and $d = 2.8$ Å.

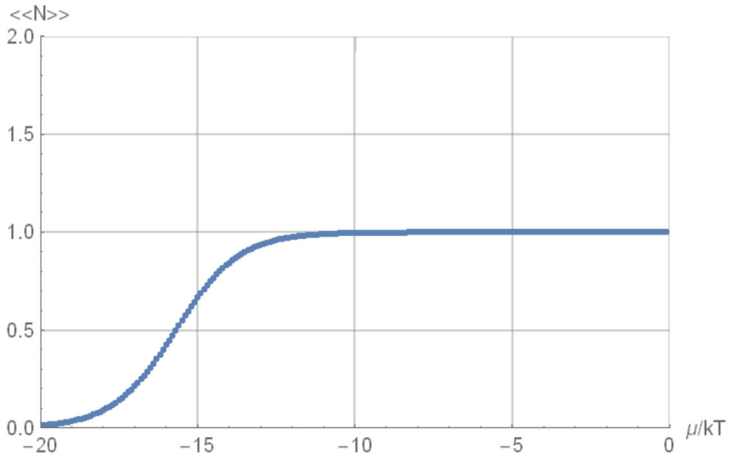

Figure 23. Adsorption isotherm predicted by equation (38) at $\varepsilon/kT = -0.5$, $\varepsilon_s/kT = -15$, $\sigma = 3.5$ Å, and $d = 2.8$ Å.

As seen from Figure 23, at the distance of $d = 2.8$ Å, the first molecule blocks the second site, and at $\mu/kT \rightarrow 0$ value of adsorption asymptotically approaches 1.

Figure 24 gives the same adsorption isotherm (as shown in Figure 23) in Ono-Kondo coordinates, Y vs. x_a, where $Y = ln\frac{x_a(1-x_b)}{x_b(1-x_a)}$ and $x_a = <<N>>/2$. As seen from equation (19), $Y = 0$ defines the point where attraction to the surface is compensated by repulsions between adsorbate molecules, i.e. where

$$\frac{\varepsilon_s}{kT} + x_a\Gamma(x_a) = 0 \tag{39}$$

Therefore, the point indicated by the arrow on Figure 24 is thermodynamic capacity, corresponding to one molecule (0.5 * 2 = 1), though geometric capacity is 2 molecules.

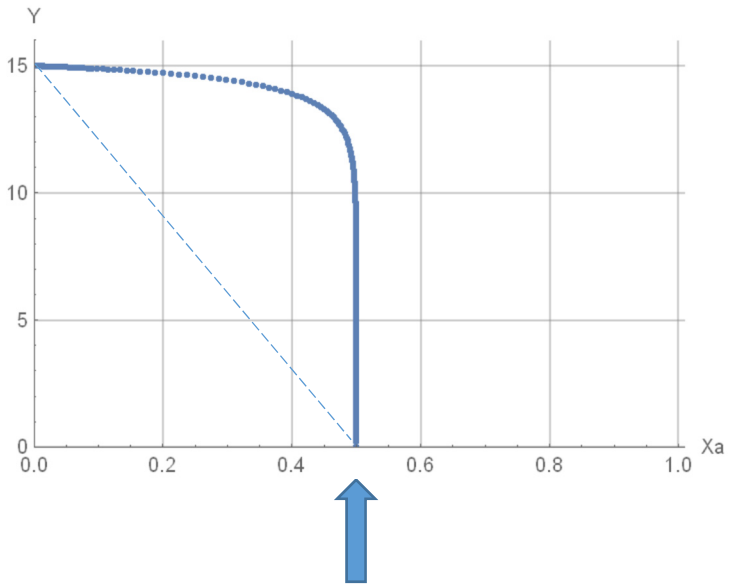

Figure 24. Adsorption isotherm predicted by equation (38) at $\varepsilon/kT = -0.5$, $\varepsilon_s/kT = -15$, $\sigma = 3.5$ Å, and $d = 2.8$ Å in coordinates Y vs. x_a. Arrow indicates thermodynamic capacity.

Equations (28) and (31) are written for cases where energy is a linear function of adsorption amount. Dashed line in Figure 24 shows a linear function $Y(x_a)$, with the same $Y(0)$ and same thermodynamic capacity (compared to the curve predicted by equation (38)). For this dashed line, $S = -30$ and $I = 15$. Therefore, equation (31) becomes

$$\ln(a_m) + 30a_m - 15 = 0 \qquad (40)$$

Solution of equation (40) gives $a_m \approx 0.52$ which is very close to the thermodynamic capacity of 0.5 for this case.

Figure 25 gives adsorption isotherm predicted by equation (38) at $\varepsilon/kT = -0.5$, $\varepsilon_s/kT = -15$, $\sigma = 3.5$ Å, and $d = 2.9$ Å.

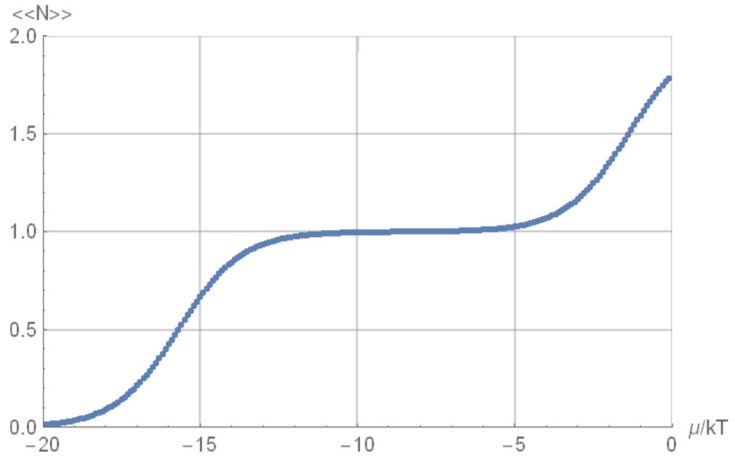

Figure 25. Adsorption isotherm predicted by equation (38) at $\varepsilon/kT = -0.5$, $\varepsilon_s/kT = -15$, $\sigma = 3.5$ Å, and $d = 2.9$ Å.

As seen from Figure 25, at the distance of $d = 2.9$ Å, the first molecule does not block the second site (just hinders), and, at $\mu/kT \rightarrow 0$, $<<N>> \approx 1.8$ molecules which gives $x_a \approx 1.8/2 = 0.9$.

Figure 26 gives the same adsorption isotherm (as shown in Figure 25) in Ono-Kondo coordinates, i.e. Y vs. x_a, where $Y = ln\frac{x_a(1-x_b)}{x_b(1-x_a)}$ and $x_a = <<N>>/2$.

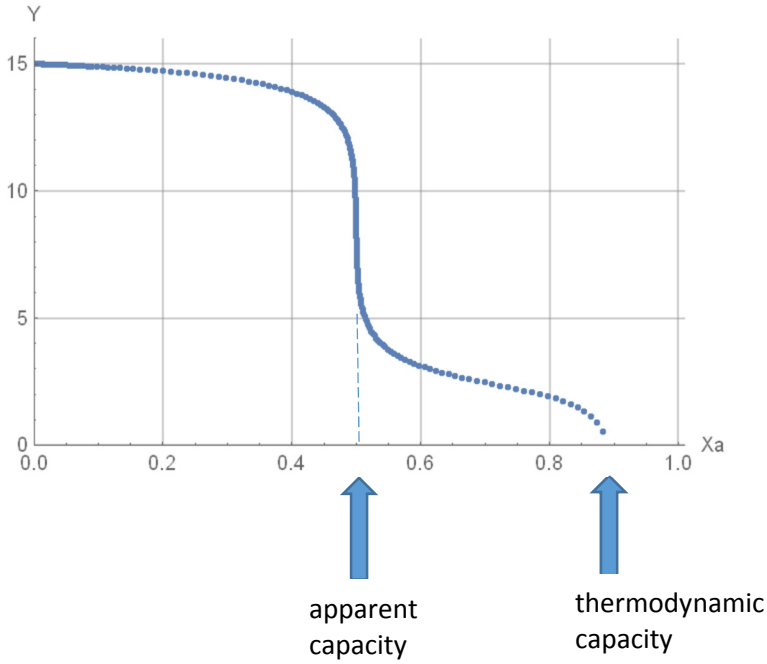

Figure 26. Adsorption isotherm predicted by equation (38) at $\varepsilon/kT = -0.5$, $\varepsilon_s/kT = -15$, $\sigma = 3.5$ Å, and $d = 2.9$ Å in coordinates Y vs. x_a. Arrows indicate apparent and thermodynamic capacities.

As seen from Figure 26, thermodynamic capacity is 0.9 which corresponds to 1.8 molecules on Figure 25 at $\mu/kT \rightarrow 0$. At $x_a = 0.5$, Figure 26 also indicates an apparent capacity of 0.5 corresponding to a plateau on Figure 25 at μ/kT between -12 and -4 where only one molecule can be adsorbed.

For the case of Figure 26, equation 40 becomes:

$$\ln(a_m) + 16.67a_m - 15 = 0 \tag{41}$$

Solution of equation (41) gives $a_m \approx 0.905$ which is very close to thermodynamic capacity of *0.9* for this case.

Figure 27 gives adsorption isotherm predicted by equation (38) at $\varepsilon/kT = -0.5$, $\varepsilon_s/kT = -15$, $\sigma = 3.5$ Å, and $d = 3.0$ Å.

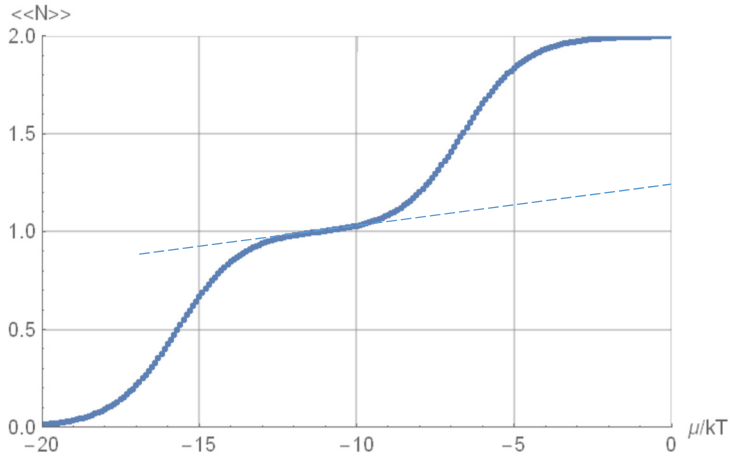

Figure 27. Adsorption isotherm predicted by equation (38) at $\varepsilon/kT = -0.5$, $\varepsilon_s/kT = -15$, $\sigma = 3.5$ Å, and $d = 3.0$ Å.

As seen from Figure 27, at $d = 3.0$ Å, for $\mu/kT \rightarrow 0$ we have $<<N>> \approx 2$ which gives $x_a \approx 1$.

Figure 28 gives the same adsorption isotherm (as shown in Figure 27) in Ono-Kondo coordinates, i.e. Y vs. x_a, where $Y = ln\frac{x_a(1-x_b)}{x_b(1-x_a)}$ and $x_a = <<N>>/2$.

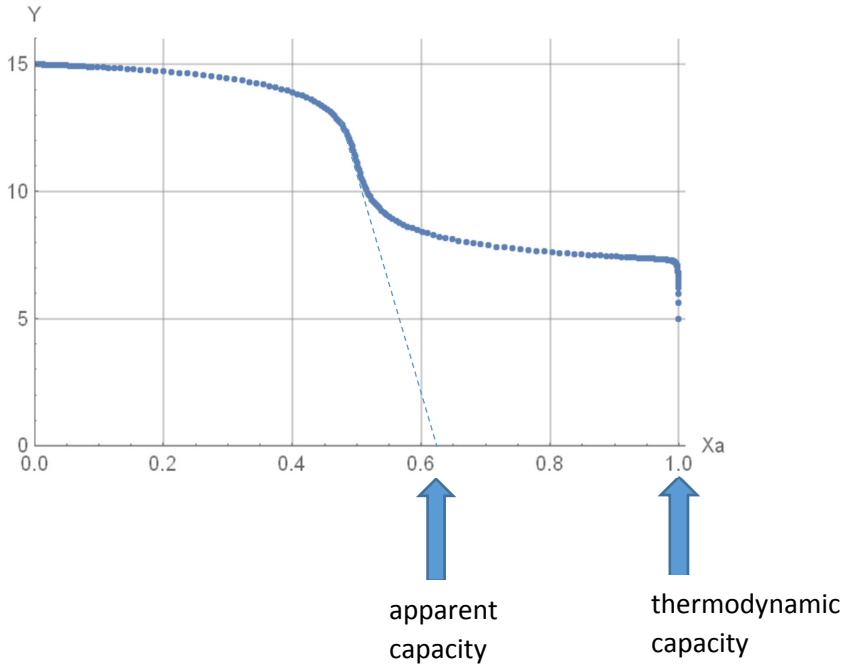

Figure 28. Adsorption isotherm predicted by equation (38) at $\varepsilon/kT = -0.5$, $\varepsilon_s/kT = -15$, $\sigma = 3.5$ Å, and $d = 3.0$ Å in coordinates Y vs. x_a. Arrows indicate apparent and thermodynamic capacities.

As seen from Figure 28, thermodynamic capacity is 1 which corresponds to 2 molecules as $\mu/kT \rightarrow 0$. Figure 28 also indicates an apparent capacity of about 0.62 corresponding to a section on Figure 27 at μ/kT between -13 and -10 (its slope is marked by the dashed line).

For the case of Figure 28, equation 40 becomes:

$$\ln(a_m) + 15a_m - 15 = 0 \qquad (42)$$

Solution of equation (42) gives $a_m = 1$ coinciding with the geometrical capacity.

*4.3. **Influence of distribution of distances between active sites***

Consider normalized Gaussian distribution of distances between active sites:

$$P(d) = q \exp\left[\frac{-(d-d_0)^2}{cd_0^2}\right] \qquad (43)$$

where d_0 is the average distance between active sites, c is the parameter characterizing width of the distribution, and q is the normalizing factor. Figure 29 illustrates dependence of distribution of distances for $d_0 = 3$ Å and $q = 1$ on parameter c.

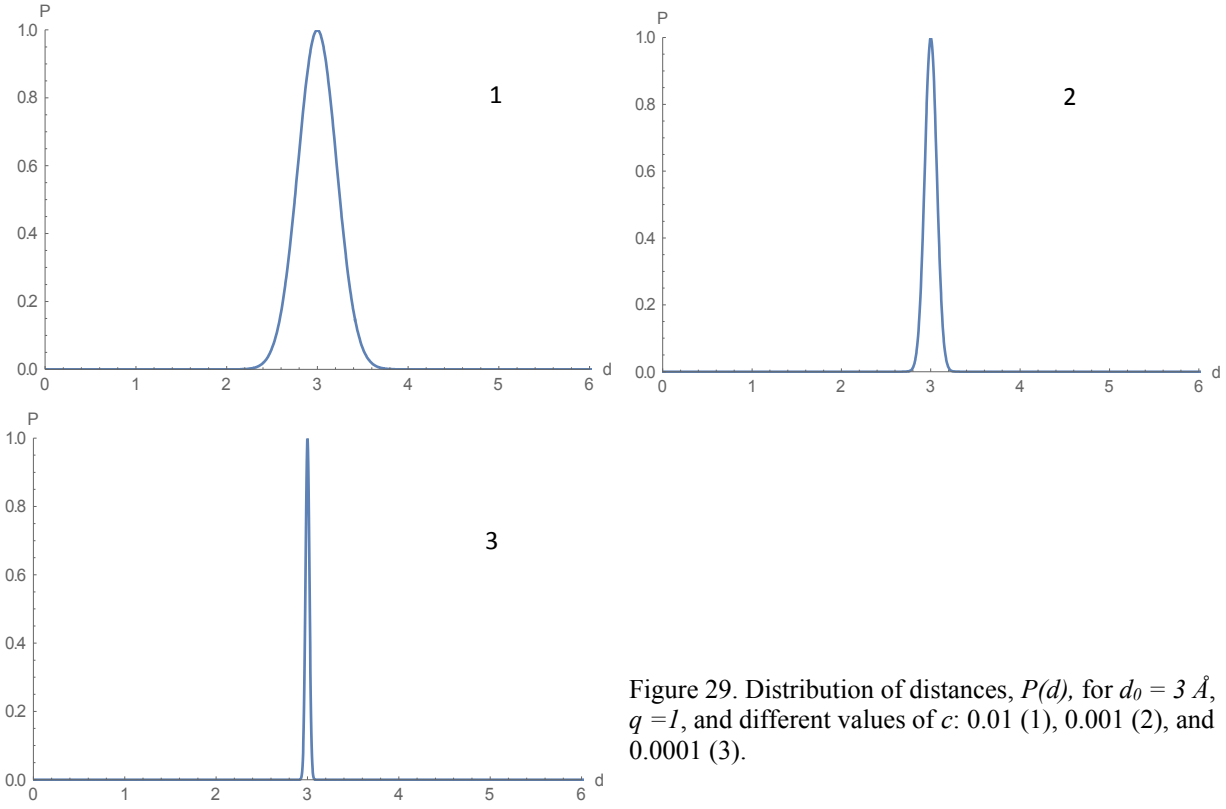

Figure 29. Distribution of distances, *P(d),* for $d_0 = 3$ Å, $q = 1$, and different values of c: 0.01 (1), 0.001 (2), and 0.0001 (3).

Taking into account equation (43), equation (38) can be rewritten in the following form:

$$<< N_{dist} >>= \frac{1}{\int_{d_1}^{d_2} P(d)d(d)} \int_{x_1}^{x_2} \frac{2\exp\left(\frac{\mu}{kT} - \frac{\varepsilon_s}{kT}\right) + 2\exp\left[\frac{2\mu}{kT} - \frac{2\varepsilon_s}{kT} - \frac{\varphi(d)}{kT}\right]}{1 + 2\exp\left(\frac{\mu}{kT} - \frac{\varepsilon_s}{kT}\right) + \exp\left[\frac{2\mu}{kT} - \frac{2\varepsilon_s}{kT} - \frac{\varphi(d)}{kT}\right]} P(d)d(d) \qquad (44)$$

Here $<<N_{dist}>>$ is the number of molecules occupying the two sites averaged over distribution of distances, and d_1 and d_2 are limits of possible distances between active sites.

Figure 30 shows adsorption isotherm predicted by equation (44) at $\varepsilon_s/kT = -15$, $\sigma = 3.5$, $d_0 = 3$ Å, $\varepsilon/kT = -0.5$, and $c = 0.0001$. Also shown in Figure 30 is adsorption isotherm without distribution of distances ($d = 3$ Å).

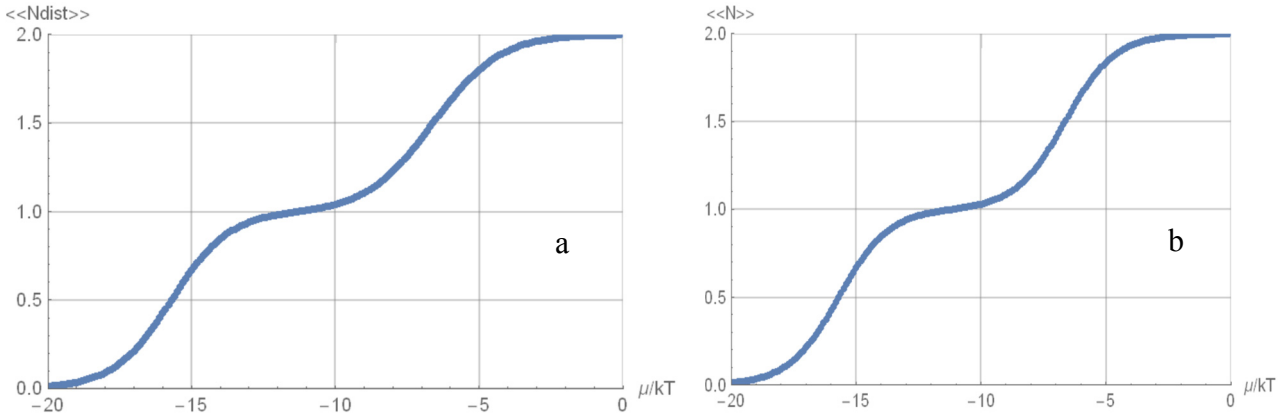

Figure 30. Adsorption isotherm predicted by equation (44) at $\varepsilon_s/kT = -15$, $\sigma = 3.5$ Å, $d_0 = 3$ Å, $\varepsilon/kT = -0.5$, and $c = 0.0001$ (frame a). Frame (b) shows adsorption isotherm for the same parameters without distribution of distances (prediction of equation (38) at $d = 3$ Å).

As seen from Figure 30, narrow distribution (c = 0.0001) results in insignificant change of adsorption isotherm.

Figure 31 shows adsorption isotherm predicted by equation (44) at $\varepsilon_s/kT = -15$, $\sigma = 3.5$, $d_0 = 3$ Å, $\varepsilon/kT = -0.5$, and $c = 0.001$. Also shown in Figure 31 is adsorption isotherm without distribution of distances ($d = 3$ Å).

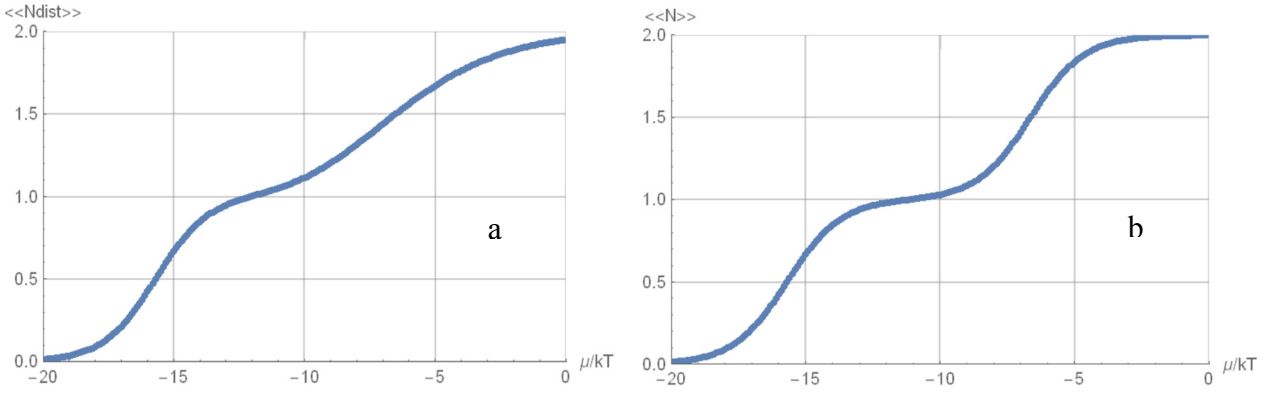

Figure 31. Adsorption isotherm predicted by equation (44) at $\varepsilon_s/kT = -15$, $\sigma = 3.5$ Å, $d_0 = 3$ Å, $\varepsilon/kT = -0.5$, and $c = 0.001$ (frame a). Frame (b) shows adsorption isotherm for the same parameters without distribution of distances (prediction of equation (38) at $d = 3$ Å).

As seen from Figure 31, wider distribution at $c = 0.001$ results in a noticeable differences in adsorption isotherm; though the main features (such as two steps and plateau between them) remain well pronounced.

Figure 32 shows adsorption isotherm predicted by equation (44) at $\varepsilon_s /kT = -15$, $\sigma = 3.5$, $d_0 = 3$ Å, $\varepsilon/kT = -0.5$, and $c = 0.01$. Also shown in Figure 32 is adsorption isotherm without distribution of distances $(d = 3$ Å$)$.

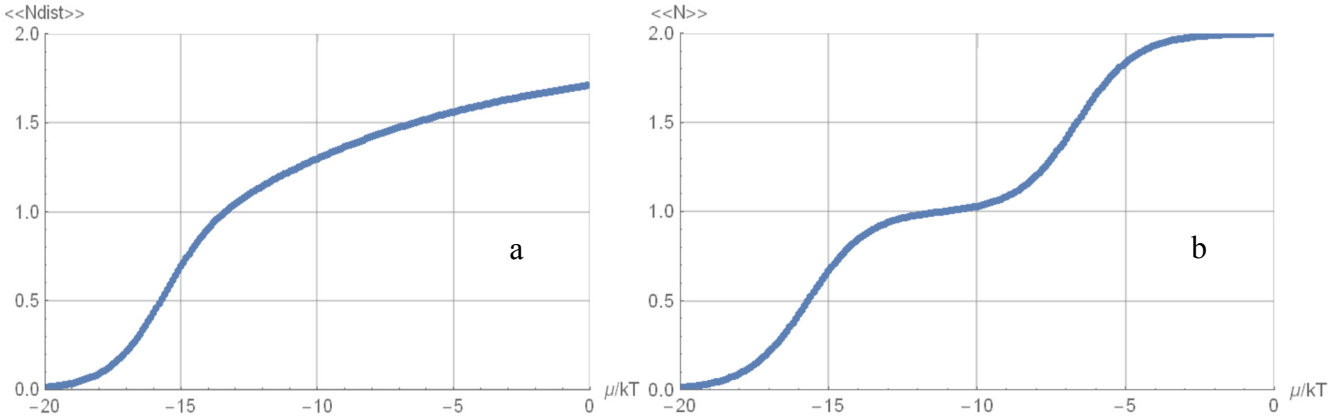

Figure 32. Adsorption isotherm predicted by equation (44) at $\varepsilon_s /kT = -15$, $\sigma = 3.5$ Å, $d_0 = 3$ Å, $\varepsilon/kT = -0.5$, and $c = 0.01$ (frame a). Frame (b) shows adsorption isotherm for the same parameters without distribution of distances (prediction of equation (38) at $d = 3$ Å).

As seen from Figure 32, wide distribution at $c = 0.01$ still results in a step at μ/kT about -15. However, the second step disappeared; instead, at μ/kT > -15, there is saturation, not reaching full capacity of $N = 2$.

Figure 33 shows adsorption isotherms for two-site model in Ono-Kondo coordinates at $\varepsilon_s /kT = -15$, $\sigma = 3.5$Å, $d_0 = 3$Å, and $\varepsilon/kT = -0.5$: (c) with distribution of distances between active sites, $c = 0.001$, and (d) with constant distance between active sites ($d = 3$ Å). Also shown are adsorption isotherms for two-site model at $\varepsilon_s /kT = -15$, $\sigma = 3.5$ Å, $d_0 = 3$ Å, and $\varepsilon/kT = -0.5$: (a) with distribution of distances between active sites, $c = 0.001$, and (d) with constant distance between active sites ($d = 3$ Å).

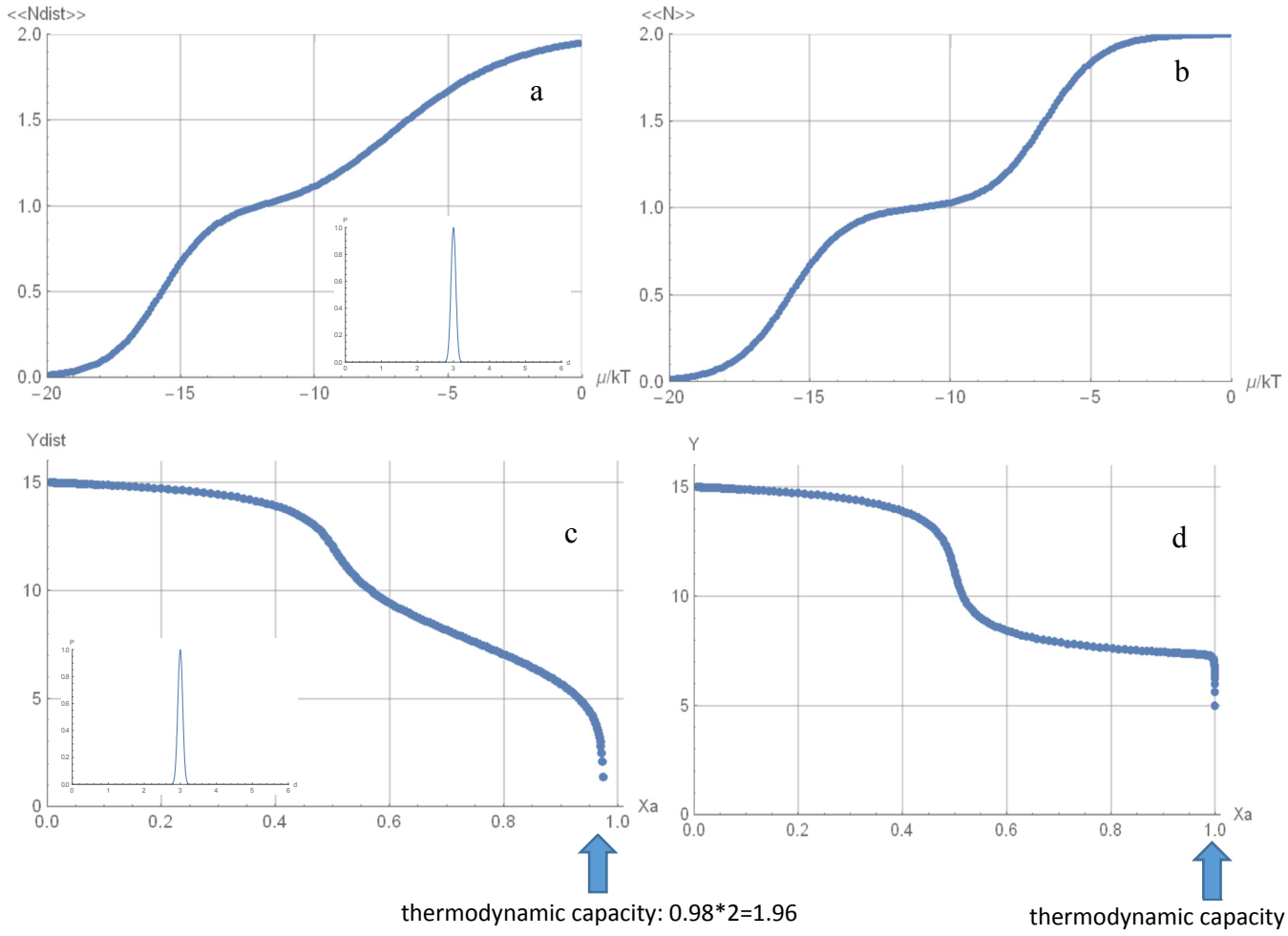

Figure 33. Adsorption isotherms for two-site model in Ono-Kondo coordinates at $\varepsilon_s/kT = -15$, $\sigma = 3.5$Å, $d_0 = 3$Å, and $\varepsilon/kT = -0.5$: (c) with distribution of distances between active sites, $c = 0.001$; (d) constant distance between active sites ($d = 3$ Å). Also shown adsorption isotherms for two-site model at $\varepsilon_s/kT = -15$, $\sigma = 3.5$ Å, $d_0 = 3$ Å, and $\varepsilon/kT = -0.5$: (a) with distribution of distances between active sites, $c = 0.001$; (b) constant distance between active sites ($d = 3$ Å).

As seen from Figure 33, distribution of distances between active sites results in a noticeable changes in adsorption isotherm. However, these changes are reflected in adsorption isotherms in Ono-Kondo coordinates in a way allowing to get information about adsorption capacity. As seen from Figure 33, frame b, adsorption capacity does not reach maximum capacity as $\mu/kT \rightarrow 0$, and this is seen from the isotherm in Ono-Kondo coordinates as $x_a \rightarrow 1$.

Figure 34 shows adsorption isotherms for two-site model in Ono-Kondo coordinates at $\varepsilon_s/kT = -15$, $\sigma = 3.5$Å, $d_0 = 3$Å, and $\varepsilon/kT = -0.5$: (c) with distribution of distances between active sites, $c = 0.01$, and (d) with constant distance between active sites ($d = 3$ Å). Also shown are adsorption isotherms for two-site model at $\varepsilon_s/kT = -15$, $\sigma = 3.5$ Å, $d_0 = 3$ Å, and $\varepsilon/kT = -0.5$: (a)

with distribution of distances between active sites, $c = 0.01$, and (d) with constant distance between active sites ($d = 3$ Å).

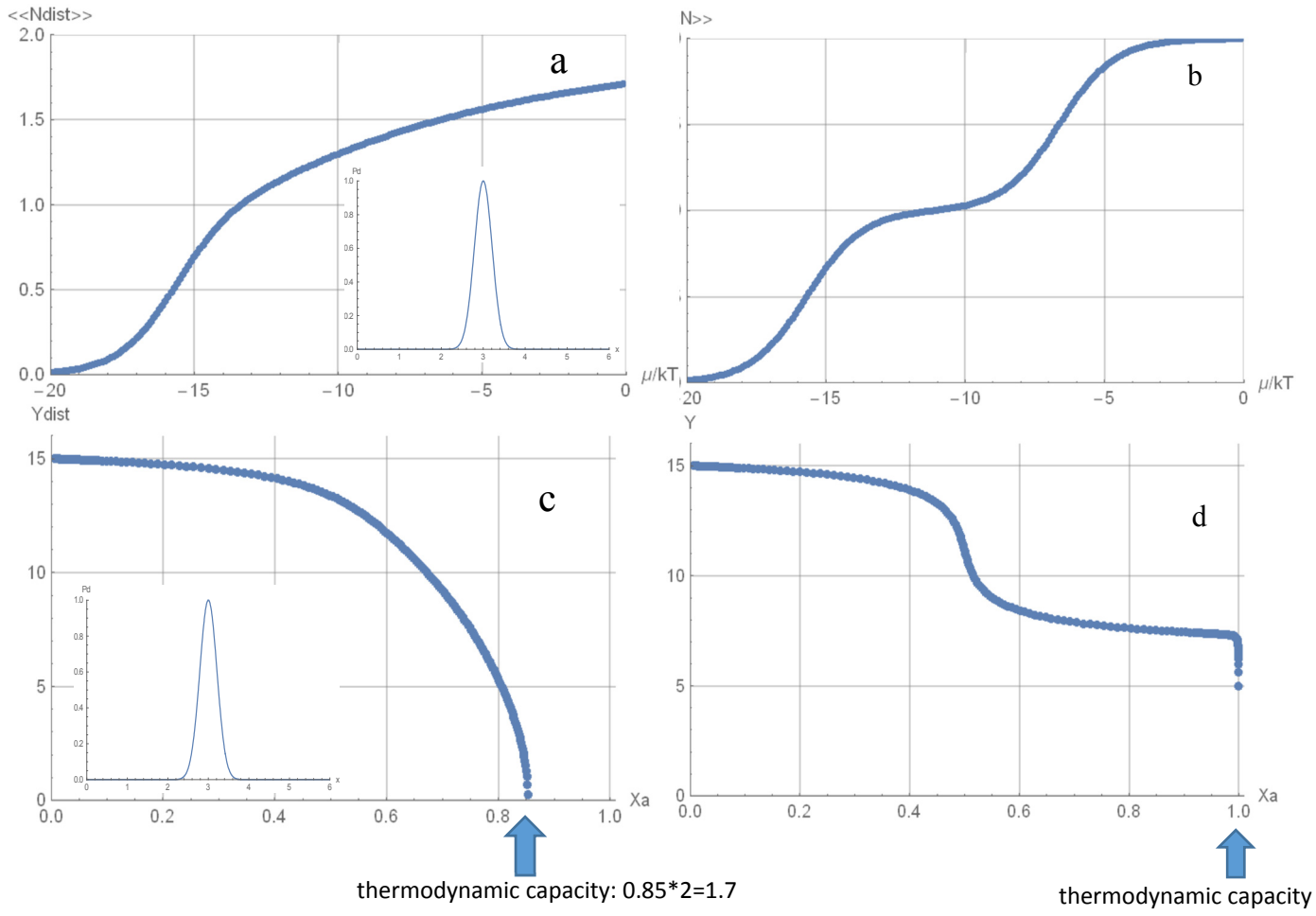

Figure 34. Adsorption isotherms for two-site model in Ono-Kondo coordinates at $\varepsilon_s/kT = -15$, $\sigma = 3.5$Å, $d_0 = 3$Å, and $\varepsilon/kT = -0.5$: (c) with distribution of distances between active sites, $c = 0.01$; (d) constant distance between active sites ($d = 3$ Å). Also shown adsorption isotherms for two-site model at $\varepsilon_s/kT = -15$, $\sigma = 3.5$ Å, $d_0 = 3$ Å, and $\varepsilon/kT = -0.5$: (a) with distribution of distances between active sites, $c = 0.01$; (b) constant distance between active sites ($d = 3$ Å).

For the case of Figure 34, equation 40 becomes $\ln(a_m) + 17.65a_m - 15 = 0$. Solution of this equation gives $a_m \approx 0.858$ which is very close to thermodynamic capacity of 0.85 indicated in Figure 34 at the point where Ydist = 0 (lower left frame). So, Ono-Kondo procedure provides correct thermodynamic capacity even at a relatively wide distribution of distances between active sites.

5. Correlation between reaction rate and adsorption compression

5.1. Correction of Langmuir-Hinshelwood model, taking into account adsorbate-adsorbate interactions

Classical theory of heterogeneous catalytic reactions is based on Langmuir-Hinshelwood (LH) mechanisms considering two major factors: a) adsorption from the gas phase, and b) thermally activated reaction on the surface. In particular, for mono- and bimolecular reactions, LH model results in the following equations for the reaction rate, *r* [25]:

$$r_m = Kx_1(x_b) \quad (45)$$

$$r_b = K[x_1(x_b)]^2 \quad (46)$$

Here, *K* is the kinetic constants of the surface reaction, and $x_1(x_b)$ is the adsorption isotherm. Kinetic constant can be determined by the Arrhenius term:

$$K = K_0 exp\left[\frac{E}{kT}\right] \quad (47)$$

where E is the activation energy and K_0 is the limit of the kinetic constant at high temperature.

Classical LH model is based on the following two assumptions:

(a) E is the minimum kinetic energy, $E_{kinetic}$, of the thermally activated molecules necessary to overcome activation barrier of the reaction, i.e.

$$E = E_{kinetic} = E_0 \quad (48)$$

where E_0 is the classical catalytic reaction barrier.

(b) adsorption isotherm can be described by Langmuir's isotherm.

However, assumption (a) takes into account only kinetic energy of the molecules and neglects their potential energy from lateral interactions. This can be fixed by including potential energy of adsorbate-adsorbate interaction, $E_{potential}$:

$$E = E_{kinetic} + E_{potential} \quad (49)$$

For adsorption compression,

$$E_{potential} = E_{rep} = z\varepsilon x_1(x_b) \quad (50)$$

where $\varepsilon > 0$ (repulsions).

Note that the values of E_{rep} for NO on zeolites (obtained in this project and given in the previous section of this report) are in the range from 4.88 kCal/mol to 5.8 kCal/mol. These

values are comparable with the typical enthalpies for catalytic reactions for NO on zeolites [26], which range from 7 kCal/mol to 9 kCal/mol.

Assumption (b) includes neglecting adsorbate-adsorbate interactions. However, our results in Figures 3, 6, 9, 10, 13, 14, 17, 18, 20, and 21 show significant deviations from the Langmuir model for all isotherms of adsorption for NO on zeolites. Straightening in Ono-Kondo coordinates demonstrates that Ono-Kondo isotherm with repulsive energy of lateral interactions is more adequate and more realistic representation of adsorption isotherms for NO on zeolites.

To generalize Langmuir-Hinshelwood model, we consider more general equation (49) instead of equation (35) for the Arrhenius term and replace Langmuir's isotherm by Ono-Kondo model taking into account lateral interactions. These improvement allow capturing essential physics of adsorbate-adsorbate interactions for catalytic reaction in adsorbed phase.

Plugging equations (49) and (50) in equations (46) and (47) gives for bimolecular reaction:

$$r_b = K_0 exp\left[\frac{E_0}{kT} + \frac{z\varepsilon}{kT} x_1(x_b)\right][x_1(x_b)]^2 \qquad (51)$$

where E_0 is the catalytic reaction barrier.

Ono-Kondo isotherm corresponding to straight lines in Figures 3, 6, 9, 10, 13, 14, 17, 18, 20, and 21 can be written in the following form:

$$x_1(x_b) = \frac{K^* x_b}{1+K^* x_b} \qquad (52)$$

where

$$K^* = \exp\left[-\frac{\varepsilon_s}{kT} - \frac{z\varepsilon}{kT} x_1(x_b)\right] \qquad (53)$$

Equations (51) – (53) determine reaction rate as a function of temperature and density of gas.

To analyze dependence of reaction rate on temperature, rewrite equation (53) in the following form:

$$kT = -\frac{z\varepsilon x_1 + \varepsilon_s}{lnK^*} \qquad (54)$$

Plugging kT from equation (54) into equation (51) gives:

$$r_b = K_0 exp\left[-\frac{(E_0 + z\varepsilon x_1) lnK^*}{(z\varepsilon x_1 + \varepsilon_s)}\right] x_1^2 \qquad (55)$$

Equations (52), (54), and (55) represent $r_b(T, x_b)$ in a parametric form with K* being a parameter.

For NO decomposition on Cu-ZSM-5, reaction activation energy is *19.5 kCal/mol* and enthalpy of adsorption of NO onto Cu+ is *-34.1 kCal/mol* [27]. Absolute value of K_0 depends on units of r_b. To plot reaction rates as functions of temperature, we used normalized reaction rate in units of conversion fraction which is equivalent to considering r_b/K_0 as a function of *T*.

Figure 35 shows dependence of reaction rate as a function of the distance between active sites, *d*, and temperature, *T*.

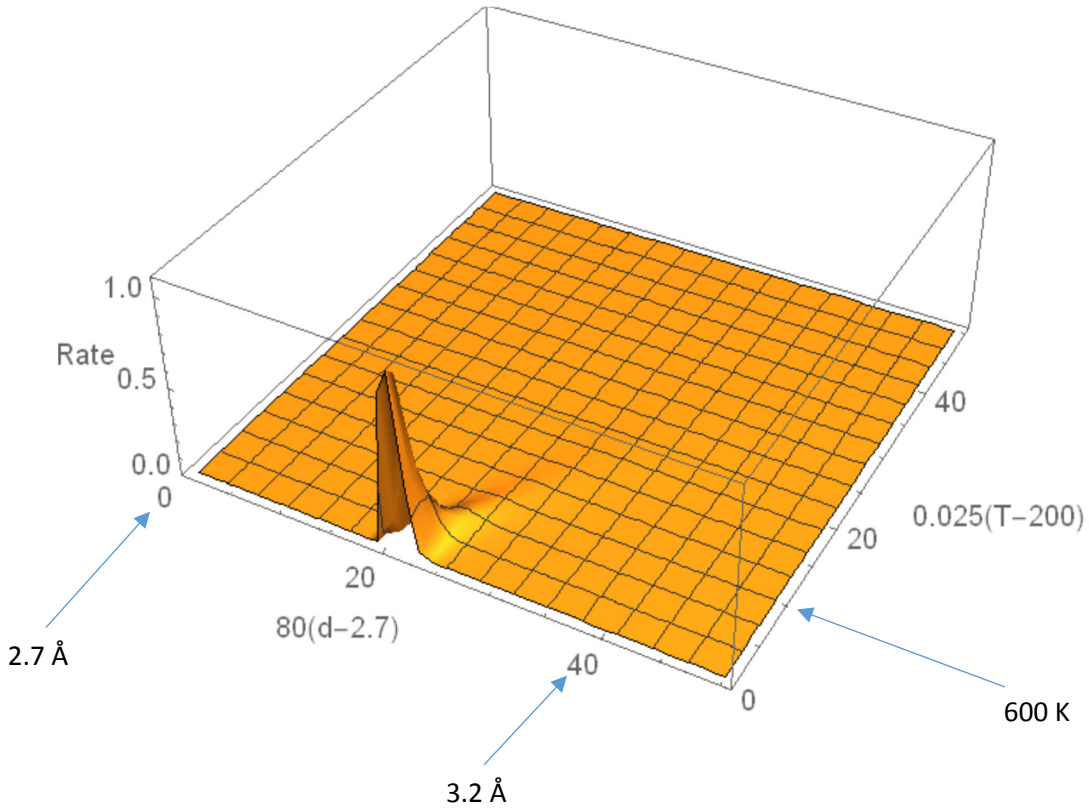

Figure 35 Dependence of reaction rate as a function of the distance between active sites, *d*, and temperature, *T*, at μ/RT = -6, ε_S/R= -12000, E_0/R=-9000, and ε_0/R = -500.

As seen from Figure 35, optimal regime (with maximum rate) is limited to a narrow range of parameters. Finding these optimal conditions is difficult without measurements of adsorption compression.

Figure 36 shows reaction rate (upper frame) and energy of adsorption compression (lower frame) as functions of the distance between active sites, *d*, and temperature, *T*, at μ/RT = -6, ε_S/R= -12000, E_0/R=-9000, and ε_0/R = -500. As seen from Figure 36, there is a correlation between maximum of reaction rate and maximum of the energy of adsorption compression.

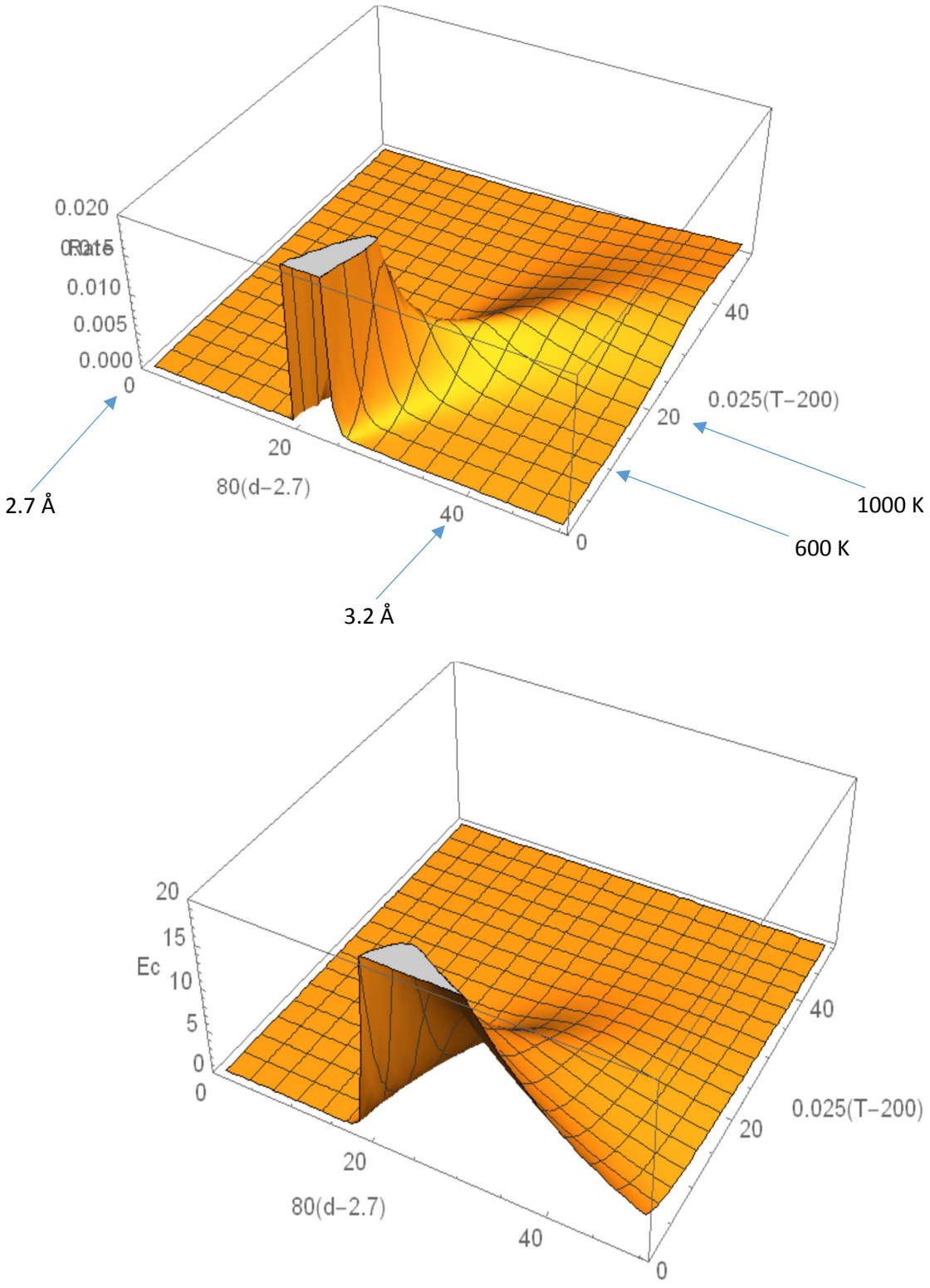

Figure 37. Reaction rate (upper frame) and energy of adsorption compression (lower frame) as functions of the distance between active sites, d, and temperature, T, at μ/RT = -6, ε_S/R= -12000, E_0/R=-9000, and ε_0/R = -500.

Figure 37 shows dependence of the reaction rate on temperature and on average distance between sites at μ/RT = -1, ε_S/R= -12000, E_0/R=-9000, and ε_0/R = -500 for Gaussian distribution of the distances between active sites.

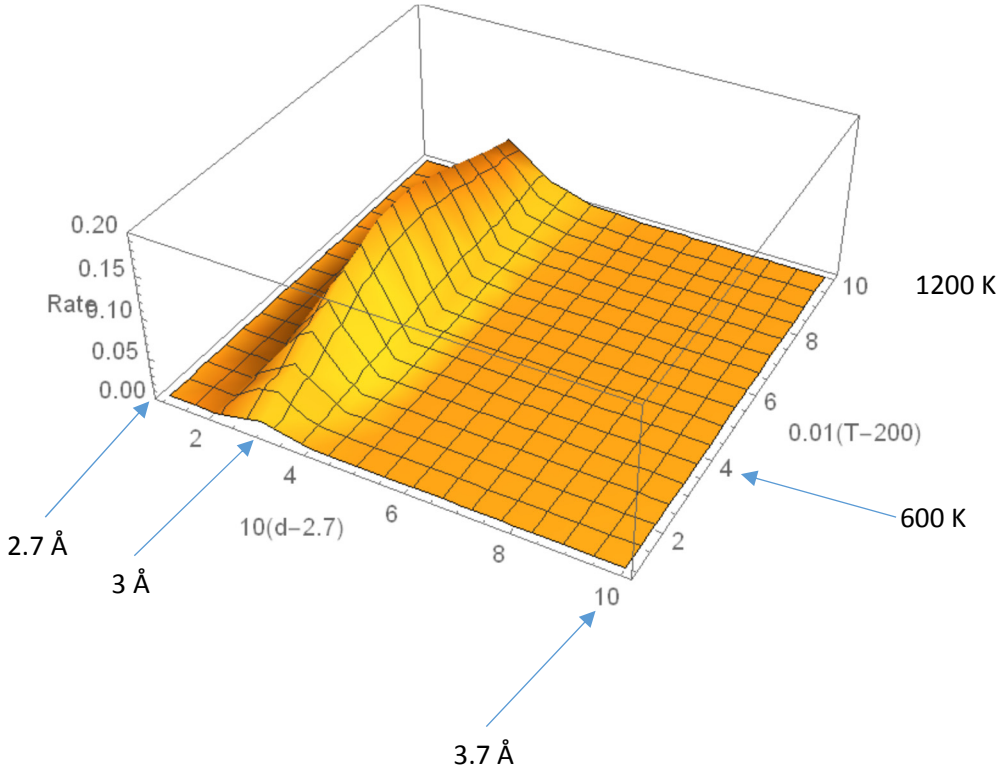

Figure 37. Dependence of the reaction rate on temperature and on average distance between sites at μ/RT = -1, ε_S/R= -12000, E_0/R=-9000, and ε_0/R = -500 for Gaussian distribution of the distances between active sites.

As seen from Figure 37, for Gaussian distribution of the distances between active sites, maximum of reaction rate is not sharp with respect to the dependence on temperature. However, it is still sharp with respect to the distance between active sites.

6. Adsorption compression indicated by adsorption measurements for NO on Cu-ZSM-5

We have analyzed parameters of corrected LH model based on comparisons with experimental data obtained in this project (presented separately in Part II). Table 3 summarizes results on comparison of corrected LH model with experimental data shown in Figures 14 – 22 of Part II. As seen from Table 3, energy of adsorption compression goes down if content of Cu goes down.

Table 3. Energy of adsorption compression as a function of copper content

Si/Al	Cu/Al	Cu/Total	Energy of Adsorption compression
11.5	0.55	0.044	9 kCal/mol
20	0.51 0.31	0.024 0.015	8.9 kCal/mol 8.7 kCal/mol
30	0.42 0.35	0.01355 0.0113	8.6 kCal/mol 8.4 kCal/mol
50	0.69 0.55	0.01353 0.01	8.4 kCal/mol 7.0 kCal/mol

Table 4 shows results of measurements of adsorbed amount for NO on Cu-ZSM-5 at 80°C.

Table 4. Adsorption isotherm for NO on Cu-ZSM-5 at 80°C.

Pressure	30 Pa	50 Pa	80 Pa	150
Normalized density, x_b	$0.24*10^{-6}$	$0.4*10^{-6}$	$0.64*10^{-6}$	$1.2*10^{-6}$
Adsorbed amount	198.65 µmol/g	305.52 µmol/g	442 µmol/g	684.9 µmol/g

Table 5 shows these data in coordinates of Ono-Kondo equation for small x_b.

Table 5. Adsorption isotherm for NO on Cu-ZSM-5 at 80°C in Ono-Kondo coordinates.

Pressure, P [Pa]	Adsorbed amount, a [µmol/g]	$ln(a/P)$	$ln(a/x_b)$
30	198.65	1.89	20.53
50	305.52	1.81	20.45
80	442	1.71	20.35
150	684.9	1.52	20.16

Figure 38 shows adsorption isotherm for NO on Cu-ZSM-5 at 80°C in Ono-Kondo coordinates, $ln(a/P)$ vs. a (upper frame) and $ln(a/x_b)$ vs. a (lower frame).

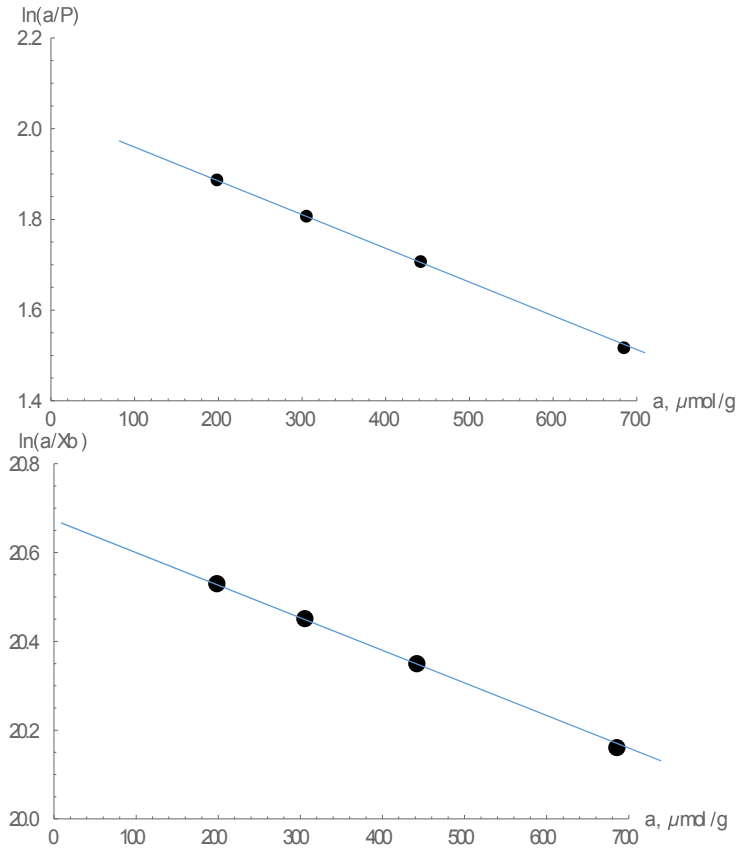

Figure 38. Adsorption isotherm for NO on Cu-ZSM-5 at 80°C in Ono-Kondo coordinates, *ln(a/P)* vs. *a* (upper frame) and $ln(a/x_b)$ vs. *a* (lower frame).

As seen from Figure 38, the slope of this isotherm in Ono-Kondo coordinates is negative which indicates adsorption compression. From the data in Table 5, we can determine the slope, $S \approx 0.00075$ and intercept, $I \approx 20.67$. Then, the following equation

$$\ln(a_m) + 0.00075 a_m - 20.67 = 0$$

gives $a_m \approx 14437\ \mu mol/g$, which allows calculation of the (repulsive) energy of adsorption compression, $E_{rep}/RT = a_m S = 14760.4 * 0.00075 \approx 11.07$, which gives, at 80°C, $E_{rep} \approx 7.8\ kCal/mol$. This result is consistent with substantial evidence that the decomposition of NO occurs on closely located ions of copper [28 – 30].

Table 6 shows results of measurements of adsorbed amount for NO on Cu-ZSM-5 at 120°C.

Table 6. Adsorption isotherm for NO on Cu-ZSM-5 at 120°C.

Pressure	80 Pa	150 Pa	200 Pa
Normalized density, x_b	$0.64*10^{-6}$	$1.2*10^{-6}$	$1.6*10^{-6}$
Adsorbed amount	352.6 µmol/g	562.8 µmol/g	685.4 µmol/g

Table 7 shows these data in coordinates of Ono-Kondo equation for small x_b.

Table 7. Adsorption isotherm for NO on Cu-ZSM-5 at 120°C in Ono-Kondo coordinates.

Pressure, *P* [Pa]	Adsorbed amount, *a* [µmol/g]	*ln(a/P)*	*ln(a/x$_b$)*
80	352.6	1.483	20.13
150	562.6	1.322	19.97
200	685.4	1.232	19.88

Figure 39 shows adsorption isotherm for NO on Cu-ZSM-5 at 120°C in Ono-Kondo coordinates, *ln(a/P)* vs. *a* (upper frame) and *ln(a/x$_b$)* vs. *a* (lower frame).

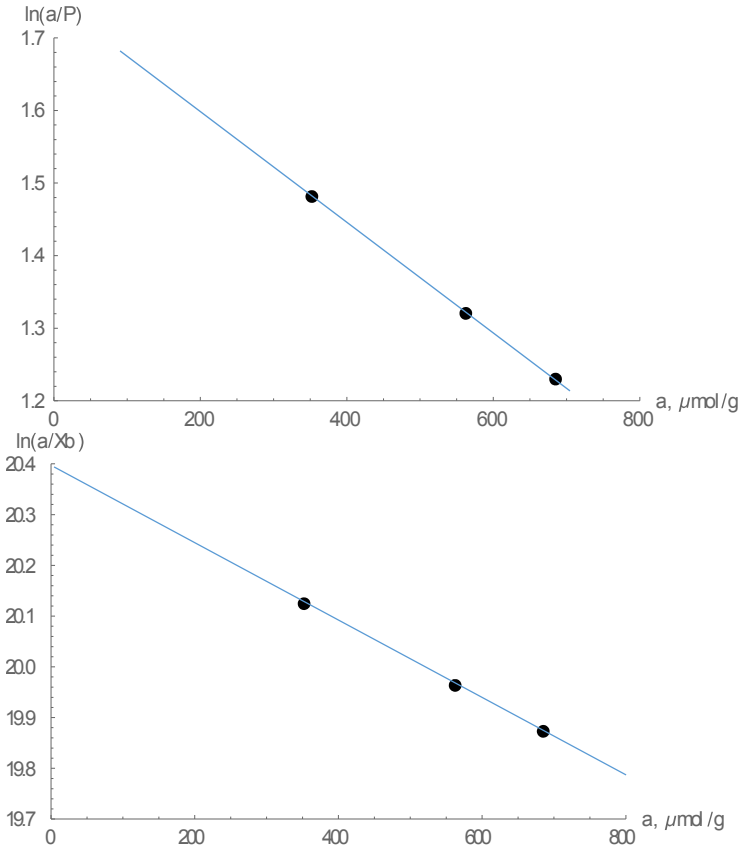

Figure 39. Adsorption isotherm for NO on Cu-ZSM-5 at 120°C in Ono-Kondo coordinates, *ln(a/P)* vs. *a* (upper frame) and $ln(a/x_b)$ vs. *a* (lower frame).

As seen from Figure 39, the slope of this isotherm in Ono-Kondo coordinates is negative which indicates adsorption compression. From the data in Table 7, we can determine the slope, $S \approx 0.00075$ and intercept, $I \approx 20.4$. Then, the following equation

$$\ln(a_m) + 0.00075a_m - 20.4 = 0$$

gives $a_m \approx 14430\ \mu mol/g$, which allows calculation of the (repulsive) energy of adsorption compression, $E_{rep}/RT = a_m S = 14430 * 0.00075 \approx 10.82$, which gives, at 120°C, $E_{rep} \approx 7.72$ *kCal/mol*. This result is consistent with substantial evidence that the decomposition of NO occurs on closely located ions of copper [28 – 30].

7. Major Results Summary

We have:

♦ Discovered a mechanism of adsorption compression in zeolites that is different from those observed previously on flat surfaces (as we have studied and Ertl observed).

♦ Measured thermodynamic adsorption capacity, a_m, of zeolites (defined where attraction to the surface is compensated by repulsions between adsorbate molecules). a_m gives a fraction of geometric (BET) surface area which is active and actually covered by adsorbate. For zeolites $a_m \approx 10\ \%$ of geometric (BET) capacity. Our results indicate the necessity for a new standard for surface areas of microporous catalysts.

♦ Measured adsorption isotherms for decomposition of NO on Cu-ZSM-5. Confirmed strong adsorption compression of NO with energies in the range of *7 kCal/mol* to *9 kCal/mol*.

♦ Measured rates of NO decomposition on Cu-ZSM-5 as function of *T* in the range from 350^oC to 550^oC. To analyze the results, we developed an Ono-Kondo correction to Langmuir-Hinshelwood (OK-LH) model taking into account adsorbate-adsorbate interactions. Comparisons of OK-LH model with our experimental data indicate that adsorption compression is a key factor in catalytic decomposition of NO on Cu-ZSM-5.

♦ Found fundamental correlation between reaction rate and adsorption compression for NO on Cu-ZSM-5, consistent with recent findings of other authors that "NO-decomposition reaction occurs on the Cu+…Cu+ pairs" [27 - 30].

8. Fundamental and Practical Implications

- We have developed a new understanding of catalytic reaction mechanisms: adsorption compression is one of the key factors;
- We have proposed a new model for catalysis kinetics, OK-LH, which takes into account adsorbate-adsorbate interactions and gives correlation between adsorption compression and reaction rate;
- We have developed a new understanding of how to design and optimize catalysts; adsorption compression can dramatically boost catalytic reactions.

9. References for Part I

1. Ono, S. and Kondo, S., "Molecular Theory of Surface Tension in Liquids", *Encyclopedia of Physics* (ed. S. Flügge), vol. 10, p. 134, Springer - Verlag, Berlin - Gottingen - Heidelberg (1960).
2. Rowlinson, J.S. and Widom, B., "Molecular Theory of Capillarity", Clarendon Press, Oxford (1982); Lane, J.E. and Johnson, C.H.J., *Aust. J. Chem.* **20**, 611 (1967).
3. Lane, J.E., *Aust. J. Chem.* **21**, 827 (1968); Altenberger, A.R. and Stecki, J., *Chem. Phys. Letters*. **5**, 29 (1970).
4. Aranovich G.L. and Donohue M.D. "ANALYSIS OF ADSORPTION ISOTHERMS: Lattice Theory Predictions, Classification of Isotherms for Gas-Solid Equilibria, and Analogy in Adsorption Behavior between Gas and Binary Liquids", *Journal of Colloid and Interface Science*, 1998, v.200, p.273-290.
5. Aranovich G.L. and Donohue M.D."Phase Loops in Density Functional Theory Calculations of Adsorption in Nano-Scale Pores", *Physical Review E,* 1999, v.60, n.5, p.5552-5560.

6. Sangwichien C., Aranovich G.L., and Donohue M.D., “Density Functional Theory Predictions of Adsorption Isotherms with Hysteresis Loops”, *Colloids and Surfaces A: Physicochemical and Engineering Aspects,* 2002, v. 206, p. 313-320.
7. Aranovich G.L. and Donohue M.D. “Lattice Density Functional Theory Predictions of Order-Disorder Phase Transitions”,*The Journal of Chemical Physics*, 2000, v. 112 (5), p. 2361-2366.
8. Aranovich G.L. and Donohue M.D. “Vapor Adsorption on Microporous Adsorbents”, *Carbon*, 2000, v.38, p. 701-708.
9. Aranovich G.L. and Donohue M.D. "Adsorption of Supercritical Fluids". *Journal of Colloid and Interface Science*, 1996, v.180, p.537-541.
10. Donohue M.D., and Aranovich G.L., “A New Classification of Isotherms for Gibbs Adsorption of Gases on Solids”, *Fluid Phase Equilibria*, 1999, v.158-160, p.557-563.
11. Aranovich G.L., and Donohue M.D. "Surface Compression in Adsorption Systems", *Colloids and Surfaces A*, 2001, v.187-188, p.95-108.
12. Sircar, S. and Myers, A.L., *AIChE Journal* 1973, v.19, 159.
13. Nakahara, T., Hirata, M., and Omori, T., *J. Chem. Eng. Data* 1974, 19, 310.
14. Talu, O. and Zwiebel, I., *AIChE Journal* 1986, v.32, 1263.
15. Hyun, S.H. and Danner, R.P. *J. Chem. Eng. Data* 1982, v.27, 196.
16. Nolan, J.T., McKeehan, T.W., and Danner, R.P., *J. Chem. Eng. Data* 1981, v.26, 112.
17. Kaul, B.K., *Ind. Eng. Chem. Res*. 1987, v.26, 928-933.
18. Szepesy, L. and Ilies, V., *Acta Chim. Hung.* 1963, v.35, 37.
19. Valenzuela, D.P. and Myers, A.L. *Adsorption Equilibrium Data Handbook*; Prentice Hall: New Jersey, 1989.
20. Yi, H., Deng, H., Tang, X., Yu, Q., Zhou, X., and Lju, H., *Journal of Hazardous Materials*, 2012, v.203-204, 111-117.
21. Deng, H., Yi, H., Tang, X., Yu, Q., Ning, P., Yang, L., *Chemical Engineering Journal*, 2012, v. 188, 77-85.
22. Coulomb, J.P., Suzanne, J., Bienfait, M., Matecki, M., Thomy, A., Croset, B., and Marti, C., J. Physique, 1980, v. 41, 1155-1164.
23. IUPAC Commission on colloid and surface chemistry including catalysis, Pure Appl. Chem. 57 (1985) 603.

24. “Recommendations for the Characterization of Porous Solids”, IUPAC Commission on Colloid and Surface Chemistry, Pure Appl. Chem. 66 (1994) 1739.
25. Davis, M. E.; Davis, R. J. Fundamentals of Chemical Reaction Engineering, Chapter 5 “Heterogeneous Catalysis”; McGraw Hill: New York, 2003.
26. Artioli, N., Lobo, R.F., and Iglesia, E., J. Phys. Chem. 2013, v.117, 20666-20674.
27. Lee, D.K., “Thermodynamic features of the Cu-ZSM-5 catalyzed NO decomposition reaction”, Korean Journal of Chemical Engineering, 2006, v. 23 (4), 547 – 554.
28. Y. Kuroda, R. Kumashiro, T. Yoshimoto, and M. Nagao, Characterization of active sites on copper ion-exchanged ZSM-5-type zeolite for NO decomposition, Phys. Chem. Chem. Phys., 1999, 1, 649-656.
29. T. Yumura, S. Hasegawa, A. Itadani, H. Kobuyashi, and Y. Kuroda, Materials, 2010, 3, 2516-2535.
30. A. Itadani, Y. Koroda, M. Tanaka, M. Nagao, Unambiguous evidence supporting the decomposition reaction of NO on two types of monovalent copper-ion in Cu-ZSM-5 zeolite, Microporous and Mesoporous Materials, 2005, 86, 159-165.
31. Aranovich G.L., and Donohue M.D., “ADSORPTION COMPRESSION: An Important New Aspect of Adsorption Behavior and Capillarity”, *Langmuir* **19**, 2722-2735 (2003).
32. Du, X. and Wu, E., “Porosity of microporous zeolites A, A, and ZSM-5 studied by small angle X-ray scattering and nitrogen adsorption”, *Journal of Physics and Chemistry of Solids* 68 (2007), pp. 1692-1699.
33. Nancy Artioli, Raul F. Lobo, and Enrique Iglesia, “Catalysis by Confinement: Enthalpic Stabilization of NO Oxidation Transition States by Micropororous and Mesoporous Siliceous Materials”, The Journal of Physical Chemistry C, 2013, v.117, pp. 20666−20674.

PART II. Demonstration of Catalysis under Adsorption Compression

1. Introduction

Nitrogen oxides (NO_x), which include nitrous oxide (N_2O), nitric oxide (NO) and nitrogen dioxide (NO_2), are some of the most dangerous exhaust gases emitted from automobile engines and industries. NO_x is responsible for acid rain, photochemical smog and harmful effects on human health. The large binding energy of N-O impedes the abatement of NO_x exhaust to occur at low temperature. Efficient catalysts for removal of NO_x is pressingly needed for meeting the future emission regulations.[1]

Copper zeolites have been investigated extensively for NO decomposition due to their excellent activity and stabilities. Direct decomposition of NO to N_2 and O_2 is a robust strategy for NO_x removal because a co-reactant is not required. Ever since the superior activity of CuZSM-5 in direct NO decomposition was discovered by Iwamoto and co-workers,[2-3] great efforts have been devoted to investigate a variety of Cu-containing zeolites, including CuFER,[4] CuZSM-11,[5-6] CuMOR,[7] CuBEA,[8] CuSSZ-13,[9] as catalysts for NO decomposition. The active sites on Cu-containing zeolites for direct NO decomposition and the associated catalytic mechanisms have been comprehensively studied. According to previous literatures,[10] one of the most widely accepted mechanisms of direct NO decomposition over Cu exchanged zeolites include two NO molecules first adsorbed on a Cu dimer site on CuZSM-5, two proximal NO molecules then react to form the N-N bond and produce intermediate N_2O, which is the rate-limiting step. The N_2O molecule reacts with the $[Cu^{2+}–O–Cu^{2+}]^{2+}$ site and subsequently form N_2 and O_2 as final products. Therefore, the distance between two Cu active sites can be critical for the formation of N-N bond. In Cu-containing zeolites prepared by ion exchange method, Cu ions are expected to connect with framework Al sites, the distances between Al sites significantly depend on Si/Al ratios or Al distributions in zeolites with different topologies. Therefore, as expected, Cu-Cu distances are different in CuZSM-5 with different Si/Al ratios or other Cu-containing zeolites. Meanwhile, it is well-known that the activity of NO decomposition on Cu-exchanged catalysts exhibited interesting “volcano-type” dependence on temperature, which is different from common reaction behavior (i.e., generally the conversion increased with increasing temperature, then reached to constant at high temperature). So far, only few works discussed this phenomenon. Iglesia et al.[11] and Lee[12] ascribed the decrease in NO decomposition

rates at high temperatures to unfavorable NO adsorption thermodynamics. However, no systematic investigation was conducted to explain the unconventional "volcano-type" behavior. Furthermore, a new adsorption model is required.

Classical and most widely used adsorption model is based on Langmuir theory,[13] which only takes adsorbate-adsorbent interactions into account and ignores adsorbate-adsorbate interactions. While adsorption compression theory and the Ono-Kondo coordinate developed by two of the current authors provided us strong tools to understand the interactions between neighboring molecules adsorbed on proximal active sites,[13] e.g. NO molecules adsorbed on Cu dimers in Cu-exchanged zeolites, which is the preliminary and rate-limitation step for NO decomposition. Since compression between two adsorbates strongly relied on the distances between them, by understanding the way that distance affecting the compression effect could help us discover the influence of distances of proximal active sites on catalytic reactions and hence develop efficient strategies to design Cu based catalysts for NO_x removal.

Herein, this annual report summarizes the progress and outcome of the research project funded by ARPA-E DE-AR0000708 in aim of investigating adsorption and compression effects of Cu-exchanged zeolites in direct NO decomposition reaction. The contents include establishment of catalytic reaction setup, synthesis and characterizations of Cu-exchanged zeolites. Reaction performance and kinetics studies of direct NO decomposition, analysis of adsorption isotherm for NO in Ono-Kondo coordinates and illustration of adsorption compression effect in direct NO decomposition over Cu-exchanged zeolites. Inspired by the study on adsorption compression of Cu dimers in Cu-exchanged zeolites, a robust Cu/CeO_2 catalyst has been developed to achieve efficient abatement of NO_x at low temperatures, preliminary data of NO decomposition over this catalyst was also provided.

2. Experimental Setup

The catalytic evaluation system was established as shown in Fig. 1. NO decomposition and isothermal NO adsorption were performed in this setup. In a typical experiment, different reactant gases were adjusted at desired ratios with mass flow controller (MFC). Catalytic reaction was conducted in the fixed-bed flow reactor at atmospheric pressure. The catalyst was

loaded into a microflow quartz reactor (7 mm i.d.) and reaction temperature was monitored by a Carbolite GERO vertical tube furnace system. To determine the conversions of reactants and the formation of products, an FTIR equipped with a 5 m gas cell and a MCT detector (Nicolet 6700, Thermo Electron Co.) as well as a gas chromatograph equipped with a BID detector (GC-2010 plus, Shimadzu) were employed. Particularly, NO, N_2O, and NO_2 were determined by FTIR at 1905 cm^{-1}, 2237 cm^{-1} and 1630 cm^{-1} respectively with resolution of 8 cm^{-1}. N_2 was determined by GC using HP-POLT Molesieve column.

Figure 1. Experimental setup of catalyst evaluation system.

3. Synthesis of Cu Substituted Zeolites

Three types of zeolites with different frameworks including Zeolite Socony Mobil–5 (ZSM-5), Mordenite (MOR) and SSZ-13 were prepared. ZSM-5 was synthesized with three Si/Al ratios: 11.5, 20 and 30. Copper was exchanged into the zeolite frameworks with ion-exchange method. The schematic illustration of zeolite preparation was shown in Fig. 2.

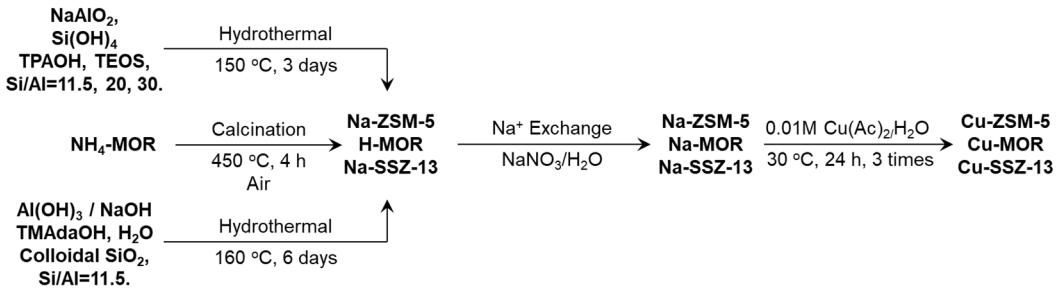

Figure 2. Schematic illustration of Cu-zeolites preparation.

The pristine ZSM-5 with different Si/Al molar ratios (Si/Al = 11.5, 20, 30, measured by X-ray fluorescence spectrum) as well as SSZ-13 (Si/Al = 11) were synthesized by hydrothermal method. Mordenite was purchased from Zeolyst Co. (CBV 21A, Si/Al = 10). The obtained zeolite frames were first thoroughly exchanged with Na^+ and then exchanged with Cu with liquid phase ion-exchange method.

3.1. Material Characterizations and Results

Scanning electron microscopy (SEM) images were taken on a JEOL 6700F field emission electron scanning microscope operating at 10.0 kV. The representative SEM image of each type of zeolite was shown in Fig. 3. ZSM-5 exhibited rectangular parallelepiped shapes with the length of 1.4 μm, and the width of 1 μm (Fig. 3a). Commercial mordenite (Si/Al = 10) exhibited small particles with the diameter of 100-200 nm, and some big granules around 400 nm can also be observed, which were aggregated by those small particles (Fig. 3b). For SSZ-13 (Si/Al = 11), the particles were individual cube-shaped crystals measuring approximately 400 nm in size, agglomerated by many smaller particles (Fig. 3c).

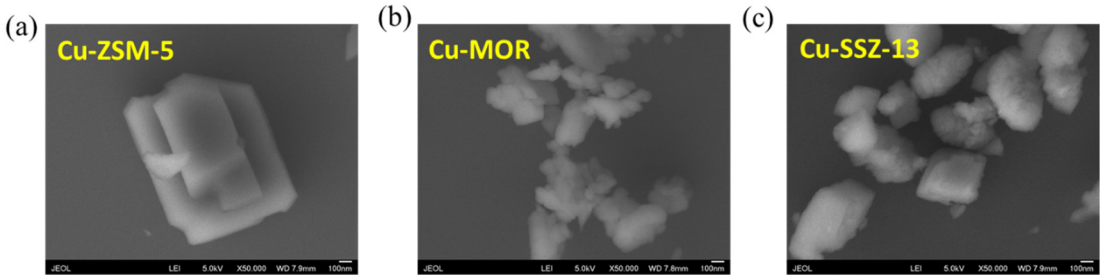

Figure 3. SEM images of (a) ZSM-5, (b) MOR-10 and (c) SSZ-13.

X-ray diffraction (XRD) patterns were obtained from a PANalytical X'Pert X-ray diffractometer equipped with a Cu Kα radiation source (λ = 1.5406 Å). Comparing XRD patterns of the samples of each zeolite with corresponding standard reference, the characteristic reflections of each zeolite topology were demonstrated, i.e. MFI (JCDPS No. 37-0359) for ZSM-5 (Fig. 4a), MOR (JCDPS No. 29-1257) for Mordenite (Fig. 4b), and CHA (JCDPS No. 47-0762) for SSZ-13 (Fig. 4c). It's also revealed in XRD patterns that ion exchanging with Cu^{2+} didn't change the crystal structures of zeolites as the diffraction patterns of Cu exchanged zeolites are almost identical to Na type zeolites. Additionally, no any Cu_2O (JCDPS No. 34-1354) or CuO (JCDPS No. 44-0706) peak can be distinguished from XRD patterns of Cu-exchanged zeolites, which indicates Cu exist as pure ionic form in zeolite pores.

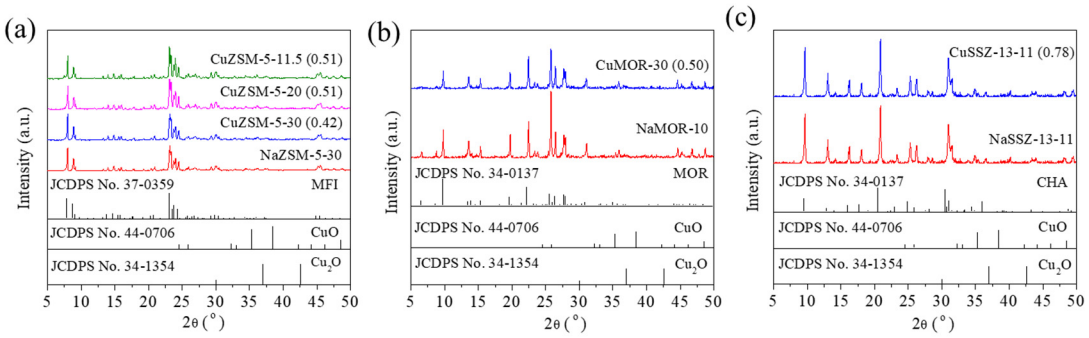

Figure 4. XRD patterns of (a) CuZSM-5 with different Si-Al ratios and Cu loadings, (b) CuMOR-10 and (c) CuSSZ-13 with comparisons to the database.

Bulk Si/Al ratios of the prepared ZSM-5 and SSZ-13 samples and commercial Mordenite were measured by X-ray fluorescence (XRF) on a Bruker-AXS S4. The Cu and Al contents were determined by inductively coupled plasma mass spectrometry (ICP-MS) using a PerkinElmer Elan DRC II Quadrupole ICP-MS after dissolution of the zeolites in HF. Nitrogen adsorption measurements were measured on a Micromeritics ASAP 2010 instrument. The samples were degassed under vacuum at 300°C for 4 h prior to the measurements. Specific surface area (SSA) was calculated using the Brunauer-Emmett-Teller (BET) theory. Table 1 summarizes the Cu content measured by ICP-MS and BET surface area measured by N_2 adsorption-desorption isotherm of each Cu zeolites.

Table 1. Summary of Cu Content and BET Surface Area of Cu-zeolites

Cu exchanged zeolites[a]	**Cu content (wt%)[b]**	**BET surface area (m^2/g)**
CuZSM-5-11.5 (0.51)	3.10	373
CuZSM-5-20 (0.51)	2.64	373
CuZSM-5-30 (0.42)	2.21	406
CuMOR-11 (0.50)	3.02	401
CuSSZ-13-11 (0.59)	3.98	593

[a] The Si/Al ratio of each zeolite was determined by XRF.

[b] The Cu content of each zeolite was measured by ICP-MS.

4. Catalytic Studies of Direct NO Decomposition and "Volcano Type" Dependence on Temperature.

Catalytic direct NO decomposition reactions over Cu exchanged zeolites were conducted in a pre-described flow reactor system at atmospheric pressure. 1 g of each Cu-zeolite (40–60

mesh) was loaded into a microflow quartz reactor as catalyst. The Cu-zeolite was pretreated at 500 ^{o}C in He before each reaction. The catalytic performance was evaluated using 500 ppm NO balanced by He and at different temperatures range from 350 ^{o}C to 550 ^{o}C. NO conversion, N_2 yield and rate of N_2 formation was evaluated with every 50 ^{o}C increment. The reaction was carried out at each temperature for at least 45 mins in order to allow reaction to reach equilibrium and conversion of NO remain constant before the measurements were taken. The NO conversion and N_2 yield were calculated using the following equations:

$$\text{NO conversion} = \frac{[NO]_{inlet}-[NO]_{outlet}}{[NO]_{inlet}} \times 100\%$$

$$N_2 \text{ yield} = \frac{2[N_2]_{outlet}}{[NO]_{inlet}-[NO]_{outlet}} \times 100\%$$

where $[NO]_{inlet}$ refers to the concentration of NO in the inlet, and $[NO]_{outlet}$ or $[N_2]_{outlet}$ refers to the concentration of NO or N_2 in the outlet. NO conversion, N_2 yield and rate of N_2 formation over each Cu-zeolite at the temperature range from 350 ^{o}C to 550 ^{o}C was shown in Fig. 5. As it's exhibited, direct NO decomposition over all Cu substituted zeolites shows typical volcano-type behavior, as the NO conversion, N_2 yield and rate of N_2 formation all reach a maximum and then decrease within the temperature range which was measured. The catalytic activity of all Cu substituted zeolites in the present study follows the trend of CuZSM-5-11.5 (0.51) > CuZSM-5-20 (0.51) > CuZSM-5-30 (0.42) > CuMOR-10(0.50) > CuSSZ-13-10 (0.59).

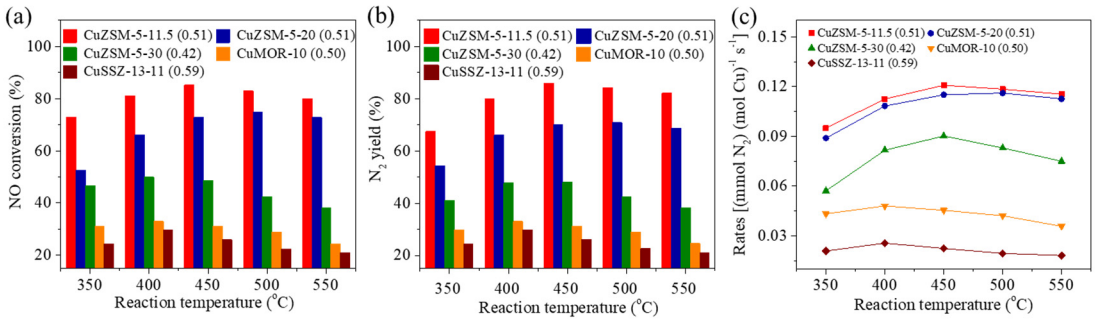

Figure 5. Catalytic activities of direct NO decomposition over different Cu-zeolites at temperatures from 350 ºC to 550 ºC. (a) NO conversions. (b) N_2 yields. (c) Rate of N_2 formation. NO concentration: 5000 ppm, balance gas: He, contact time: 0.05 min*g_{catal}/ml.

5. Kinetics Studies of Direct NO Decomposition over Cu Substituted Zeolites

Fig. 6 showed the Arrhenius plot of NO decomposition over different Cu-exchanged zeolites. The apparent activation energy (E_{app}) could be obtained from the slope in the Arrhenius plot where (ln$K$) was plotted against the reciprocal temperature (Fig. 6a). Comparing the apparent activation energies over different Cu-exchanged zeolites, it is obvious that activation energies in low temperature followed the sequence of CuZSM-5-11.5 (0.51) < CuZSM-5-20 (0.51) < CuZSM-5-30 (0.42) < CuMOR-10 (0.50) < CuSSZ-13-10 (0.59), which suggests that adsorption-compression effect is beneficial to facilitate catalytic NO decomposition over Cu-Cu dimers at low temperature (T < 400 ºC). Meanwhile, the apparent activation energies at high temperature followed the invertible sequence of CuZSM-5-11.5 (0.51) > CuZSM-5-20 (0.51) > CuZSM-5-30 (0.42) > CuMOR-10 (0.50) > CuSSZ-13-10 (0.59), suggesting that adsorption-compression plays a prohibitive role in catalytic direct NO decompositions at high temperature (T > 400 ºC).

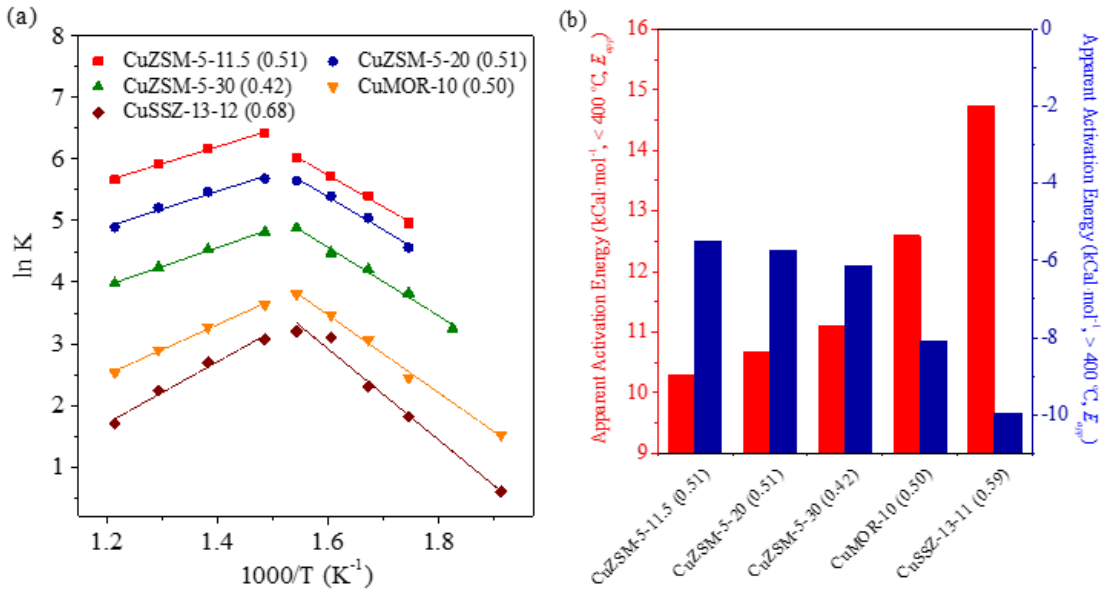

Figure 6. (a) Arrhenius plot of apparent activation energies of direct NO decomposition over different Cu-zeolites. (b) Calculated apparent activation energies at low temperature (T<400 ºC, red) and high temperature (T>400 ºC, blue) regimes of direct NO decomposition over different Cu-zeolites.

6. Isothermal NO Adsorption Measurements

Isothermal NO adsorption on different Cu-containing zeolites catalysts was conducted in the fixed-bed flow reactor at atmospheric pressure. The same pretreatment (He, 500 ºC) was implemented. After pretreatment, the temperature was cooled down to 80 ºC under pure He atmosphere and kept the temperature at 80 ºC for adsorption measurement. The feed concentrations of NO were adjusted to 300 ppm, 500 ppm, 800 ppm and 1500 ppm by mixing pure He and 0.5% NO/He gas. The NO/He mixture (201 h^{-1}) was fed to the catalyst. The composition of the effluent stream was continuously monitored for the entire length of the experiment until all concentrations of different gas species (NO, N_2O, N_2) were stable. The detection system was the same experimental setup as above. The measured outlet concentration

of NO, N_2O and N_2 in the time on stream during NO isothermal adsorptions of different NO concentrations on CuZSM-5-11.5 (0.51) at 80 ºC was chosen as an example and was shown in Fig. 7. The amount of NO adsorbed on the catalyst at the end of the adsorption measurement was evaluated by measuring the overall uptake of NO and the quantities of N_2O, NO_2 and N_2 transiently produced, as follows:

$$NO_{ads} = NO_{uptake} - 2N_2O_{prod} - 2\,N_{2,\,prod} - NO_{hold\ up}$$

where:

NO_{ads} represents NO totally adsorbed (as calculated from mass balance in the gas phase);

NO_{uptake} represents the amount of NO consumed (directly measured in the gas phase);

N_2O_{prod} represents the amount of N_2O produced (directly measured in the gas phase);

$N_{2,\,prod}$ represents the amount of N_2 produced (directly measured in the gas phase);

$NO_{hold\ up}$ represents the amount of NO necessary to fill the dead volumes of the experimental set-up (evaluated in the opportune blank tests).

The amounts of these adsorbed species were estimated by integrating the corresponding signals as a function of time; all these quantities are reported in Table 2 for CuZSM-5-11.5 (0.51).

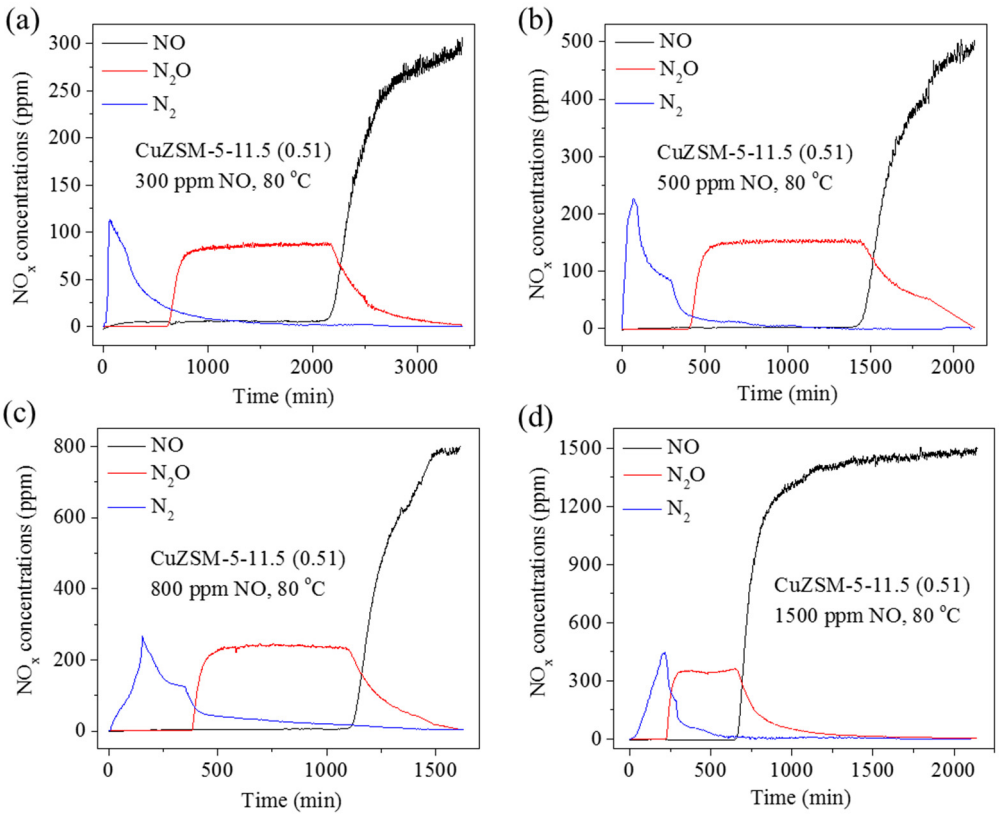

Figure 7. Outlet concentrations of NO, N_2O and N_2 during NO isothermal adsorptions of different NO concentrations on CuZSM-5-11.5 (0.51) at 80 ºC. (a) 300 ppm NO. (b) 500 ppm NO. (c) 800 ppm NO. (d) 1500 ppm NO.

Table 2. Amounts of Gaseous Species Evaluated by the Integration of the Signals during the Adsorption of Different Concentrations of NO on CuZSM-5-11.5 (0.51) in Ono-Kondo Coordinates.

Concentrations of NO	NO_{ads}	NO_{uptake}	N_2O_{prod}	N_{2prod}	$NO_{hold\ up}$
	μmol g^{-1}	μmol g^{-1}	μmol g^{-1}	μmol g^{-1}	μmol g^{-1}
300 ppm	199	527	125	36	6
500 ppm	305	703	154	40·	10
800 ppm	441	903	160	63	16
1500 ppm	686	1188	170	70	22

The compression energies can be calculated followed the principles introduced in the previous section from the slopes in Fig. 8, which had been listed in Table 3 and related to the average Cu-Cu distances of each Cu substituted zeolites measured by XAFS techniques in previous literature with very similar Cu loadings and Si/Al ratios. It can be found that calculated compression energy followed the sequence of CuZSM-5-11.5 (0.51) > CuZSM-5-20 (0.51) > CuZSM-5-30 (0.42) > CuMOR-10 (0.50) > CuSSZ-13-10 (0.59), which agrees well with catalytic activity at low temperature regime (T<400 ºC).

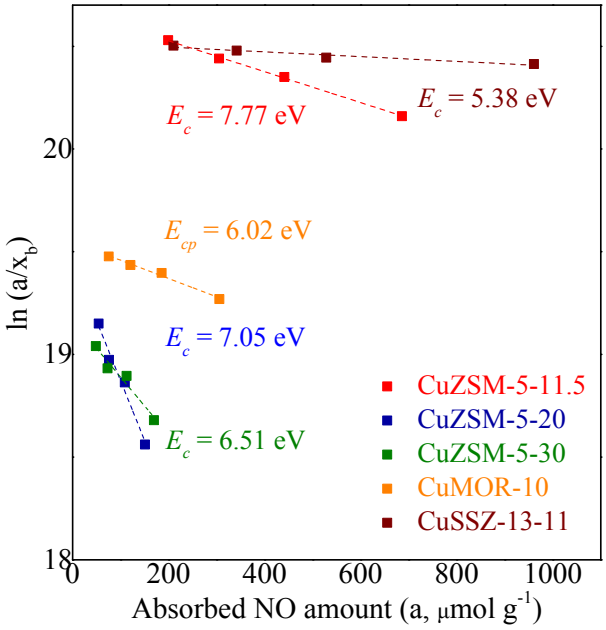

Figure 8. Adsorption isotherms for NO on Cu-Zeolites at 80 ºC in Ono-Kondo coordinates.

Table 3. Summary of Compression Energy Calculated from Ono-Kondo Coordinates and Average Cu-Cu Distances of Cu Dimers in Cu Zeolites in Present Study

Catalysts	Cu···Cu distances (Å)	Compression Energy (kCal mol^{-1})[f]
CuZSM-5-11.5 (0.51)	2.84[a]	7.77
CuZSM-5-20 (0.51)	2.94[b]	7.05
CuZSM-5-30 (0.42)	3.13[c]	6.51
CuMOR-11 (0.50)	3.34[d]	6.02

CuSSZ-13-11 (0.59)	3.76[e]	5.38

[a] J. Am. Chem. Soc. 125 (2003) 7629-7640

[b] J. Phys. Chem. 98 (1994) 10832-10846

[c] Catal. Lett. 5 (1990) 189-196

[d] J. Mater. Chem. 7 (1997) 1917–1923

[e] J. Phys. Chem. C 116 (2012) 4809-4818

[f] Obtained from NO isothermal adsorption measurements

7. Effect of Cu···Cu Dimer Distances on Catalytic Activity of NO Decomposition over Cu Substituted Zeolites

By plotting the calculated compression energy at T < 400 ºC versus Cu-Cu distance (Fig. 9a), it can be revealed that shorter Cu-Cu distance gave rise to larger compression energy in Cu-exchanged zeolites. Also, by plotting the rate of N_2 formation at T < 400 ºC versus compression energy (Fig. 9b), we can see the rate of N_2 formation increases as compression energy increases. Hence, it can be concluded that the calculated compression energy is bridged to the average Cu-Cu distance of each Cu-zeolite, which is crucial for catalytic activity of direct NO decomposition.

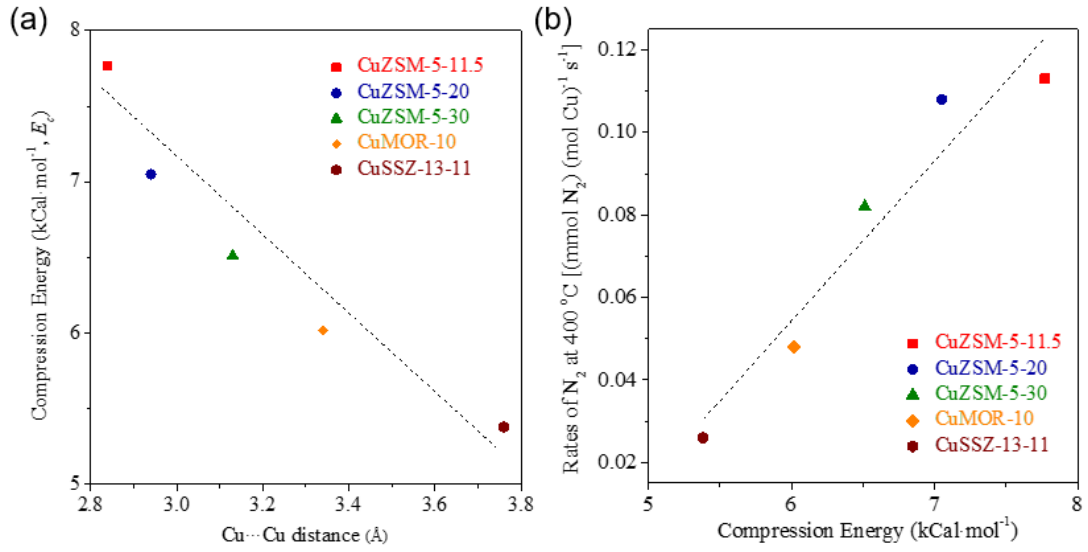

Figure 9. (a) Dependence of compression energy on Cu-Cu distance. (b) Dependence of rates of N_2 formation at 400 °C on compression energy.

8. Preliminary Results for NO Decomposition over Cu/CeO_2

Recently, a series of research works demonstrated that cerium oxide can provide oxygen vacancies for absorption and release of oxygen as well as the regeneration of catalytic active sites, which is ideal for NO_x decomposition.[15,16] Inspired by the conclusion of our studies on Cu-zeolites and previous literatures, it is believed CeO_2 can serve as a better support for Cu(I) dimers, which can give rise to robust catalytic ability in NO decomposition. To the best of our knowledge, no catalyst which can achieve direct NO decomposition at room temperature has yet been reported. Here as shown in Fig. 10, we report the excellent performance of a 5% Cu/CeO_2 catalyst which was capable of achieve direct NO decomposition at room temperature with almost 100% conversion and 100% selectivity to N_2 and O_2. The catalyst was active for more than 400 min. If CO as a reducing agent was introduced, the catalyst was able to reach steady state, 100% conversion of NO and 100% selectivity to N_2 was achieved at 100 °C (Fig. 11). Systematic

investigation of this catalyst is undergoing, details of catalyst preparation and experiments were kept confidential.

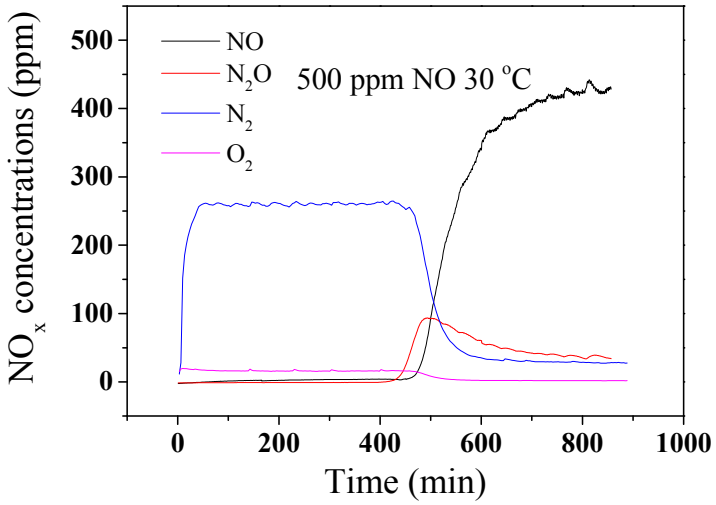

Figure 10. Performance of direct NO decomposition over 5% Cu/CeO_2 at 30 °C.

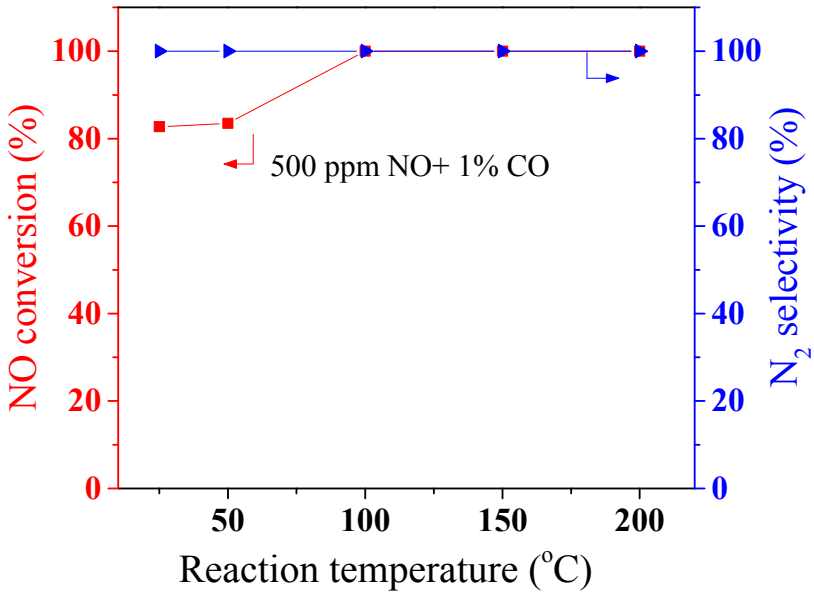

Figure 11. Performance of NO+CO reaction over 5% Cu/CeO_2.

9. Comparisons with experimental data on rate vs. temperature for NO on Cu-ZSM-5

Figure 12 shows reaction rate as a function of temperature predicted by equations (51)-(53) of Part I for E_0 *=19.5 kCal/mol*, ε_s *= 34.1 kCal/mol*, x_b *= 0.001*, z *= 2*, K_0 *= 3*, and different values of ε: *9 kCal/mol* (1) and *0* (2). Also shown in Figure 12 are experimental points for NO on zeolite ZSM-5 at Si/Al = 11.5 and Cu/Al = 0.55.

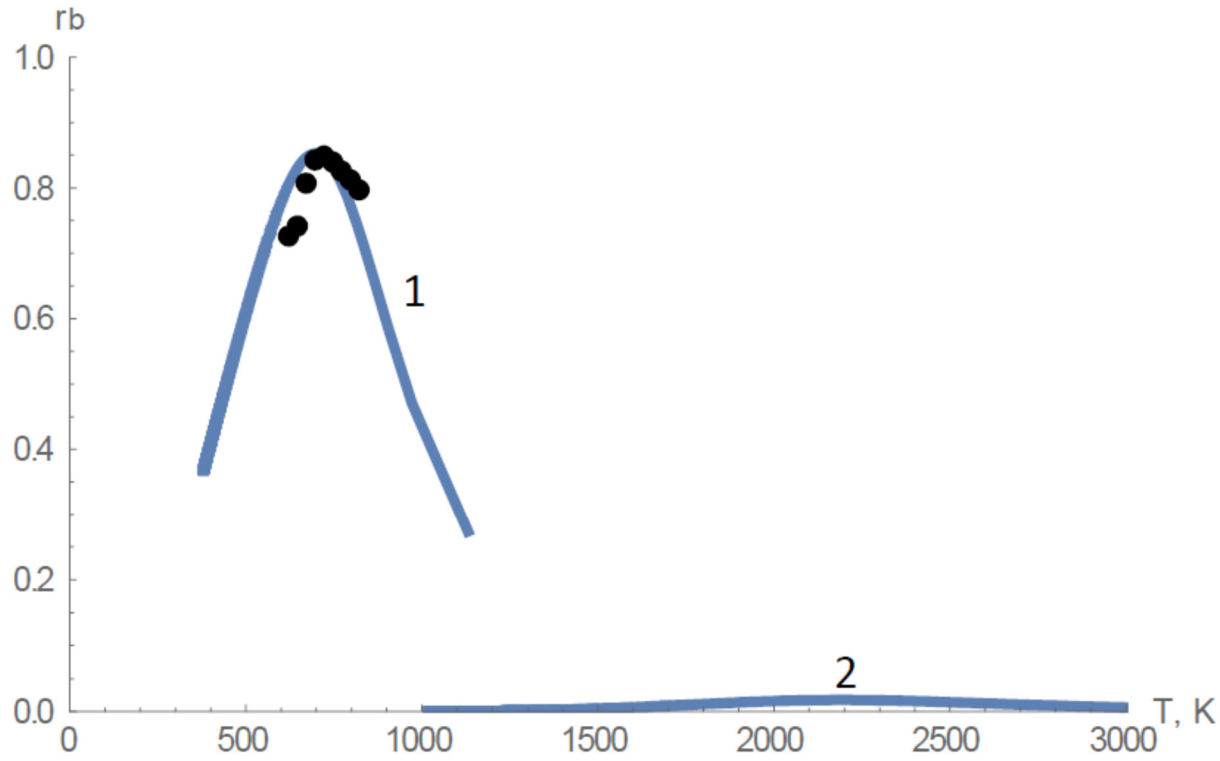

Figure 12. Reaction rate, r_b, as a function of temperature predicted by equations (51)-(53) of Part I for E_0 *=19.5 kCal/mol*, ε_s *= 34.1 kCal/mol*, x_b *= 0.001*, z *= 2*, K_0 *= 3,* and different values of ε: *9 kCal/mol* (1) and *0* (2). Also shown are experimental points for NO on zeolite ZSM-5 at Si/Al = 11.5 and Cu/Al = 0.55.

As seen from Figure 12, without adsorption compression (at $\varepsilon = 0$) reaction rate is very small. However, at $\varepsilon = 9$ *kCal/mol* , reaction rate goes up dramatically and predictions of equations (51)-(53) of Part I are in agreement with the experimental data.

Figure 13 shows reaction rate as a function of temperature predicted by equations (51)-(53) of Part I for E_0 *=19.5 kCal/mol*, ε_s *=34.1 kCal/mol*, x_b *=0.001*, z *=2*, K_0 *=3,* and $\varepsilon = 8.9$ *kCal/mol*. Also shown in Figure 13 are experimental points for NO on zeolite ZSM-5 at Si/Al = 20 and Cu/Al = 0.51.

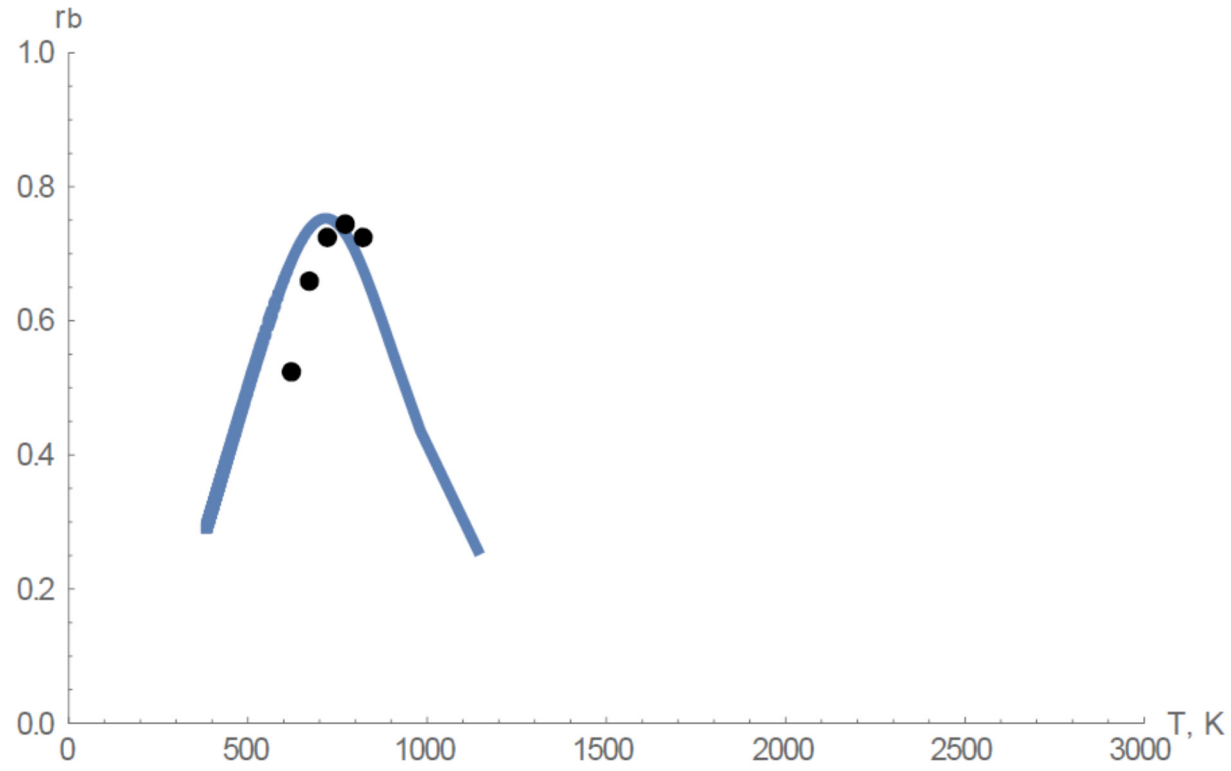

Figure 13. Reaction rate, r_b, as a function of temperature predicted by equations (51)-(53) of Part I for E_0 =*19.5 kCal/mol*, ε_s = *34.1 kCal/mol*, x_b = *0.001*, z = *2*, K_0 = *3,* and ε = *8.9 kCal/mol* . Also shown are experimental points for NO on zeolite ZSM-5 at Si/Al = 20 and Cu/Al = 0.51.

As seen from Figure 13, at ε = *8.9 kCal/mol* predictions of equations (51)-(53) of Part I are in reasonably good agreement with the experimental data for NO on zeolite ZSM-5 at Si/Al = 20 and Cu/Al = 0.51. The difference between Figures 12 and 13 can be explained by slight decrease of distance between ions of Cu+ for Si/Al =11.5 and Cu/Al =0.55 compared to Si/Al =20 and Cu/Al =0.55.

Figure 14 shows reaction rate as a function of temperature predicted by equations (51)-(53) of Part I for E_0 =*19.5 kCal/mol*, ε_s = *34.1 kCal/mol*, x_b = *0.001*, z = *2*, K_0 = *3,* and ε = *8.7 kCal/mol*. Also shown in Figure 14 are experimental points for NO on zeolite ZSM-5 at Si/Al = 20 and Cu/Al = 0.31.

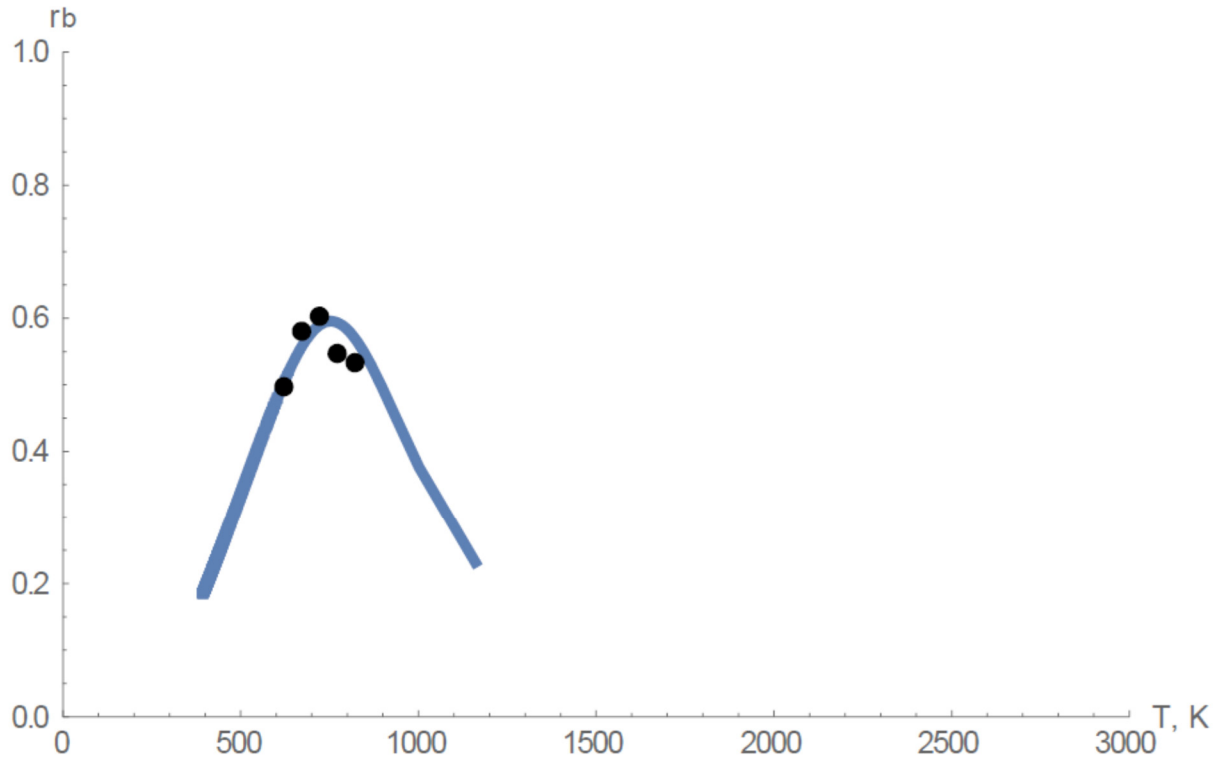

Figure 14. Reaction rate, r_b, as a function of temperature predicted by equations (51)-(53) for E_0 =19.5 *kCal/mol*, ε_s = *34.1 kCal/mol*, x_b = *0.001*, z = *2*, K_0 = *3,* and ε = *8.7 kCal/mol*. Also shown are experimental points for NO on zeolite ZSM-5 at Si/Al = 20 and Cu/Al = 0.31.

Figures 15 – 18 give reaction rates as functions of temperature predicted by equations (51)-(53) of Part I for E_0 =*19.5 kCal/mol*, ε_s = *34.1 kCal/mol*, x_b = *0.001*, z = *2*, and K_0 = *3.* In Figure 15, ε = *8.6 kCal/mol* and experimental points are for NO on zeolite ZSM-5 at Si/Al = 30 and Cu/Al = 0.42. In Figure 16, ε = *8.4 kCal/mol* and experimental points are for NO on zeolite ZSM-5 at Si/Al = 30 and Cu/Al = 0.35. In Figure 17, ε = *8.4 kCal/mol* and experimental points are for NO on zeolite ZSM-5 at Si/Al = 50 and Cu/Al = 0.69. In Figure 18, ε = *7.0 kCal/mol* and experimental points are for NO on zeolite ZSM-5 at Si/Al = 50 and Cu/Al = 0.55.

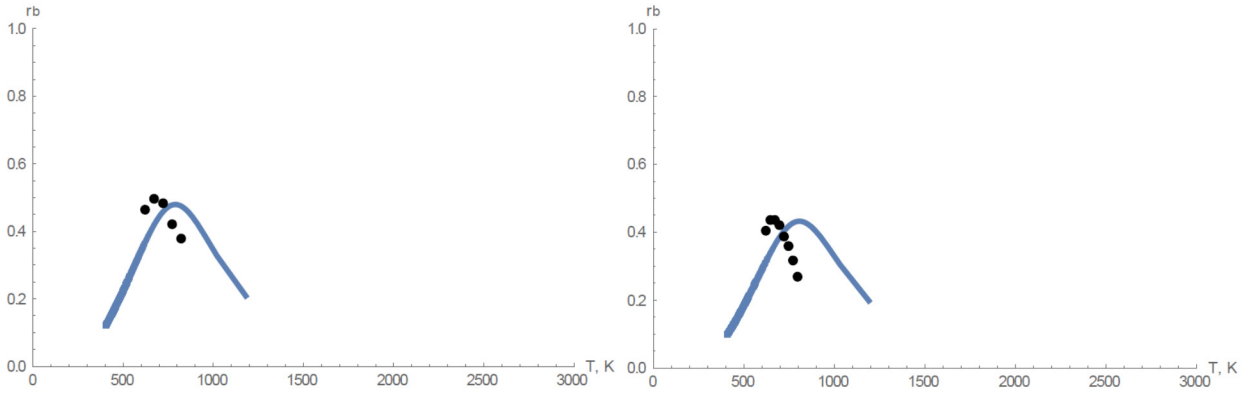

Figure 15 (left frame). Reaction rate, r_b, as a function of temperature predicted by equations (51)-(53) of Part I for E_0 =19.5 kCal/mol, ε_s = 34.1 kCal/mol, x_b = 0.001, z = 2, K_0 = 3 and ε = 8.6 kCal/mol. Also shown are experimental points for NO on zeolite ZSM-5 at Si/Al = 30 and Cu/Al = 0.42.

Figure 16 (right frame). Reaction rate, r_b, as a function of temperature predicted by equations (51)-(53) of Part I for E_0 =19.5 kCal/mol, ε_s = 34.1 kCal/mol, x_b = 0.001, z = 2, K_0 = ,3 and ε = 8.4 kCal/mol. Also shown are experimental points for NO on zeolite ZSM-5 at Si/Al = 30 and Cu/Al = 0.35.

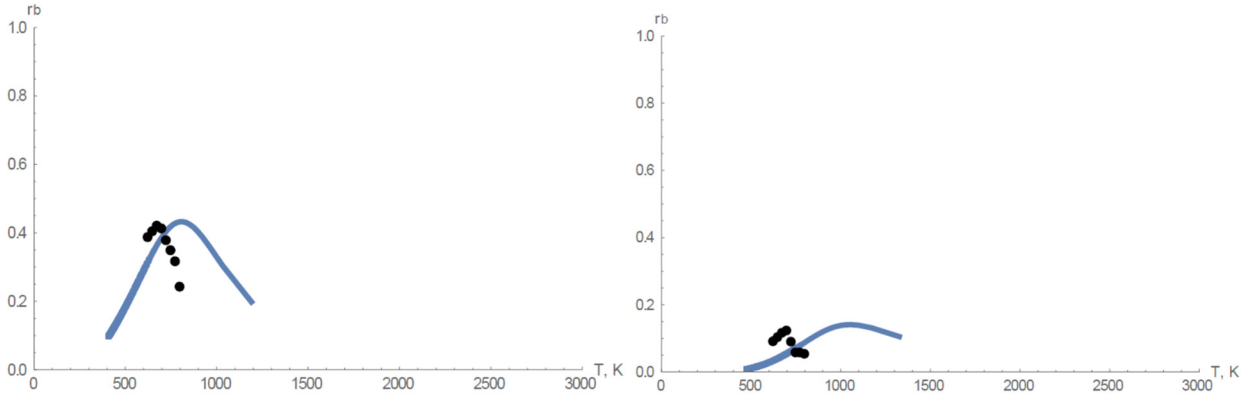

Figure 17 (left frame). Reaction rate, r_b, as a function of temperature predicted by equations (51)-(53) of Part I for E_0 =19.5 kCal/mol, ε_s = 34.1 kCal/mol, x_b = 0.001, z = 2, K_0 =3, and ε = 8.4 kCal/mol. Also shown are experimental points for NO on zeolite ZSM-5 at Si/Al = 50 and Cu/Al = 0.69.

Figure 18 (right frame). Reaction rate, r_b, as a function of temperature predicted by equations (51)-(53) of Part I for E_0 =19.5 kCal/mol, ε_s = 34.1 kCal/mol, x_b = 0.001, z = 2, K_0 = 3, and ε = 7.0 kCal/mol. Also shown are experimental points for NO on zeolite ZSM-5 at Si/Al = 50 and Cu/Al = 0.55.

As seen from Figures 15 – 18, at low concentration of Cu, experimental points are shifted toward lower temperatures. In our opinion, this is because, at lower concentration of copper, some ions of copper are oxidized and become Cu^{2+}, and this changes ε_s . Enthalpy of adsorption onto oxidized Cu^{2+} is 27.8 kCal/mol (see Ref. [27] of Part I). If we use the average between 34.1

kCal/mol (Cu^{+}) and 27.8 kCal (Cu^{2+}) (which gives about 31 kCal/mol), agreement between theory and experiment becomes much better. This is illustrated on Figures 19 – 22 with normalization factor $K_0 = 4.6$).

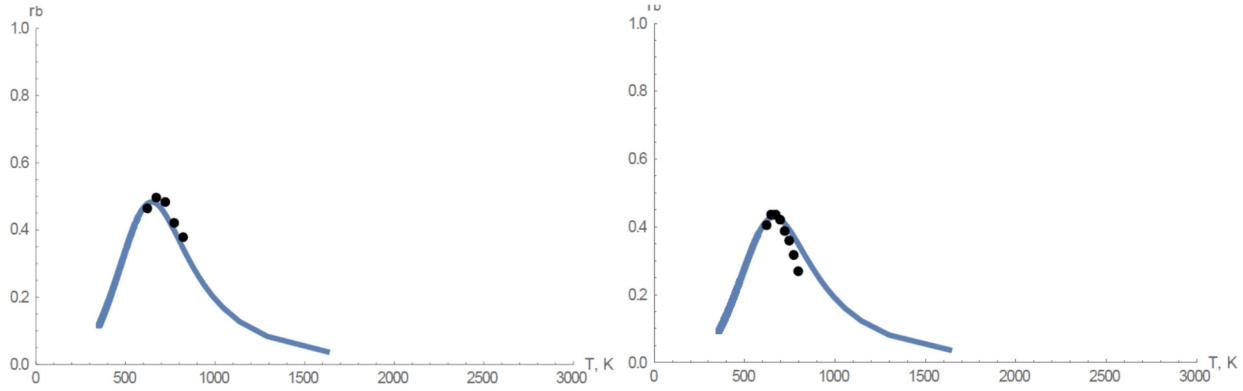

Figure 19 (left frame). Reaction rate, r_b, as a function of temperature predicted by equations (51)-(53) of Part I for $E_0 = 19.5$ *kCal/mol*, $\varepsilon_s = 31$ *kCal/mol*, $x_b = 0.001$, $z = 2$, $K_0 = 4.6$, and $\varepsilon = 8.6$ *kCal/mol*. Also shown are experimental points for NO on zeolite ZSM-5 at Si/Al = 30 and Cu/Al = 0.42.

Figure 20 (right frame). Reaction rate, r_b, as a function of temperature predicted by equations (51)-(53) of Part I for $E_0 = 19.5$ *kCal/mol*, $\varepsilon_s = 31$ *kCal/mol*, $x_b = 0.001$, $z = 2$, $K_0 = 4.6$, and $\varepsilon = 8.4$ *kCal/mol*. Also shown are experimental points for NO on zeolite ZSM-5 at Si/Al = 30 and Cu/Al = 0.35.

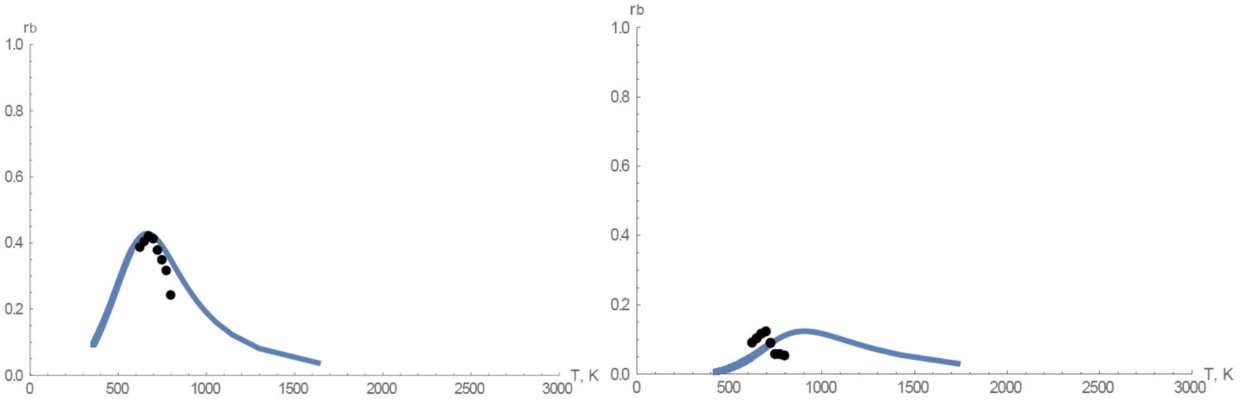

Figure 21 (left frame). Reaction rate, r_b, as a function of temperature predicted by equations (51)-(53) of Part I for $E_0 = 19.5$ *kCal/mol*, $\varepsilon_s = 31$ *kCal/mol*, $x_b = 0.001$, $z = 2$, $K_0 = 4.6$, and $\varepsilon = 8.4$ *kCal/mol*. Also shown are experimental points for NO on zeolite ZSM-5 at Si/Al = 50 and Cu/Al = 0.69.

Figure 22 (right frame). Reaction rate, r_b, as a function of temperature predicted by equations (51)-(53) of Part I for $E_0 = 19.5$ *kCal/mol*, $\varepsilon_s = 31$ *kCal/mol*, $x_b = 0.001$, $z = 2$, $K_0 = 4.6$, and $\varepsilon = 7.0$ *kCal/mol*. Also shown are experimental points for NO on zeolite ZSM-5 at Si/Al = 50 and Cu/Al = 0.55.

10. References for Part II

1. National Archives and Records Administration, Fed. Regist. **2016,** 81, 73478–74274.
2. Iwamoto, M.; Furukawa, H.; Mine, Y.; Uemura, F.; Mikuriya, S. I.; Kagawa, S., Copper(Ii) Ion-Exchanged Zsm-5 Zeolites as Highly-Active Catalysts for Direct and Continuous Decomposition of Nitrogen Monoxide. *J Chem Soc Chem Comm* **1986,** (16), 1272-1273.
3. Iwamoto, M.; Yahiro, H.; Mizuno, N.; Zhang, W. X.; Mine, Y.; Furukawa, H.; Kagawa, S., Removal of Nitrogen Monoxide through a Novel Catalytic Process .2. Infrared Study on Surface-Reaction of Nitrogen Monoxide Adsorbed on Copper Ion-Exchanged Zsm-5 Zeolites. *J Phys Chem-Us* **1992,** *96* (23), 9360-9366.
4. Attfield, M. P.; Weigel, S. J.; Cheetham, A. K., On the nature of nonframework cations in a zeolitic deNO(x) catalyst - A synchrotron X-ray diffraction and ESR study of Cu-ferrierite. *J Catal* **1997,** *172* (2), 274-280.
5. Kustova, M. Y.; Rasmussen, S. B.; Kustov, A. L.; Christensen, C. H., Direct NO decomposition over conventional and mesoporous Cu-ZSM-5 and Cu-ZSM-11 catalysts: Improved performance with hierarchical zeolites. *Appl Catal B-Environ* **2006,** *67* (1-2), 60-67.
6. Xie, P. F.; Ma, Z.; Zhou, H. B.; Huang, C. Y.; Yue, Y. H.; Shen, W.; Xu, H. L.; Hua, W. M.; Gao, Z., Catalytic decomposition of N2O over Cu-ZSM-11 catalysts. *Micropor Mesopor Mat* **2014,** *191*, 112-117.
7. Granger, P.; Parvulescu, V. I., Catalytic NOx Abatement Systems for Mobile Sources: From Three-Way to Lean Burn after-Treatment Technologies. *Chem Rev* **2011,** *111* (5), 3155-3207.
8. Mihai, O.; Widyastuti, C. R.; Andonova, S.; Kamasamudram, K.; Li, J. H.; Joshi, S. Y.; Currier, N. W.; Yezerets, A.; Olsson, L., The effect of Cu-loading on different reactions involved in NH3-SCR over Cu-BEA catalysts. *J Catal* **2014,** *311*, 170-181.
9. Paolucci, C.; Parekh, A. A.; Khurana, I.; Di Iorio, J. R.; Li, H.; Caballero, J. D. A.; Shih, A. J.; Anggara, T.; Delgass, W. N.; Miller, J. T.; Ribeiro, F. H.; Gounder, R.; Schneider, W. F., Catalysis in a Cage: Condition-Dependent Speciation and Dynamics of Exchanged Cu Cations in SSZ-13 Zeolites. *J Am Chem Soc* **2016,** *138* (18), 6028-6048.
10. Sajith, P. K.; Shiota, Y.; Yoshizawa, K., Role of Acidic Proton in the Decomposition of NO over Dimeric Cu(I) Active Sites in Cu-ZSM-5 Catalyst: A QM/MM Study. *Acs Catal* **2014,** *4* (6), 2075-2085.

11. Moden, B.; Da Costa, P.; Fonfe, B.; Lee, D. K.; Iglesia, E., Kinetics and mechanism of steady-state catalytic NO decomposition reactions on Cu-ZSM5. *J Catal* **2002,** *209* (1), 75-86.
12. Lee, D. K., Thermodynamic features of the Cu-ZSM-5 catalyzed NO decomposition reaction. *Korean J Chem Eng* **2006,** *23* (4), 547-554.
13. Aranovich, G. L.; Donohue, M. D., Adsorption compression: An important new aspect of adsorption behavior and capillarity. *Langmuir* **2003,** *19* (7), 2722-2735.
14. Aranovich, G. L.; Donohue, M. D. Phase Loops in Density-Functional-Theory Calculations of Adsorption in Nanoscale Pores. *Phys. Rev. E - Stat. Physics, Plasmas, Fluids, Relat. Interdiscip. Top.* **1999**, *60* (5), 5552–5560.
15. Zabilskiy, M.; Djinović, P.; Tchernychova, E.; Pintar, A. N2O Decomposition over CuO/CeO2catalyst: New Insights into Reaction Mechanism and Inhibiting Action of H2O and NO by Operando Techniques. *Appl. Catal. B Environ.* **2016**, *197*, 146–158.
16. Zabilskiy, M.; Djinović, P.; Tchernychova, E.; Tkachenko, O. P.; Kustov, L. M.; Pintar, A. Nanoshaped CuO/CeO2 Materials: Effect of the Exposed Ceria Surfaces on Catalytic Activity in N2O Decomposition Reaction. *ACS Catal.* **2015**, No. October, 5357–5365.